KARADENİZ TECHNICAL UNIVERSITY
THE GRADUATE SCHOOL OF NATURAL AND APPLIED SCIENCES

DEPARTMENT OF CIVIL ENGINEERING

EFFECT OF ACCIDENTAL JOINT ECCENTRICITY ON THE BEHAVIOR OF CONCENTRIC BRACES

MASTER THESIS

Necip SANNAH

JANUARY 2024
TRABZON

KARADENİZ TECHNICAL UNIVERSITY
THE GRADUATE SCHOOL OF NATURAL AND APPLIED SCIENCES

DEPARTMENT OF CIVIL ENGINEERING

EFFECT OF ACCIDENTAL JOINT ECCENTRICITY ON THE BEHAVIOR OF CONCENTRIC BRACES

Necip SANNAH

This thesis is accepted to give the degree of
"MASTER OF SCIENCE"
By The Graduate School of Natural and Applied Sciences at Karadeniz Technical University

The Date of Submission	**: 28 / 12 / 2023**
The Date of Examination	**: 22 / 01 / 2024**

Supervisor : Assoc. Prof. Serhat DEMİR

Trabzon 2024

ACKNOWLEDGMENTS

I would like to express my first words of thanks and praise to Allah, the almighty, for the many blessings and the strength provided to me throughout the course of working on this thesis.

I am grateful to my supervisor, Assoc. Prof. Dr. Serhat DEMİR, whose mentorship and guidance have been significant in helping me advance in my academic career. From the moment I began my research, he provided invaluable support and I consider myself fortunate having the opportunity to work under his enlightening supervision.

Heartfelt appreciation is extended to my wonderful mother, supportive father and my dear brothers. Their unconditional support and patience have been constant throughout the highs and lows of my studies. Their sacrifice and belief in my potential form the bedrock of my strength, significantly contribute to my academic achievements. Their impact on my life extends far beyond mere support.

I extend special thanks to my beloved wife, Fatma, for the endless love and the moral support she provided throughout this research.

Last but not least I want to thank Yılmaz YILMAZ and Hussien SOALIH for their helpful support in every aspect. Your assistance is greatly appreciated.

Necip SANNAH
Trabzon 2024

DECLARATION

I hereby declare that I have completed this study entitled "Effect of Accidental Joint Eccentricity on The Behavior of Concentric Braces", which I submitted as a Master Thesis, under the supervision of my advisor, Assoc. Prof. Serhat DEMİR, from start to finish. I confirm that I collected the data/samples myself, conducted the experiments/analyses in relevant laboratories or supervised them, and accurately presented any information obtained from other sources in both the text and the references. I further confirm that I complied with scientific research and ethical standards during the study process and acknowledge that I will accept any legal consequences in case of any violations be discovered. 22/01/2024

Necip SANNAH

TABLE OF CONTENTS

Master Thesis

SUMMARY

EFFECT OF ACCIDENTAL JOINT ECCENTRICITY ON THE BEHAVIOR OF CONCENTRIC BRACES

Necip SANNAH

Karadeniz Technical University
The Graduate School of Natural and Applied Sciences
Civil Engineering Graduate Program
Supervisor: Assoc. Prof. Serhat DEMİR
2024, 76 Pages

Concentric braces are designed based on the assumption that they have concentrically loaded joints. To avoid eccentricity at a joint, the line of action of the load from each member framing into a joint should intersect at the joint centroid. However, compression members in real structures are not perfectly straight, aligned, or concentrically loaded as is assumed in design calculations. In AISC 360-22 and EC 1993, certain safety factors applied to consider uncertainties related to initial imperfections of concentric braces. However, these safety factors are the same for each slenderness ratio, and it is not known up to which eccentricity level they provide a safe result. Based on these shortcomings, an experimental and numerical program was carried out to examine the effect of various accidental joint eccentricity conditions on the behavior of concentric braces. Results showed that the effect of joint eccentricity on the buckling strength of concentric braces varies according to the slenderness ratio. According to experimental and numerical studies, the influence of joint eccentricity begins to be insignificant when the normalized slenderness ratio is greater than 1.5. However, when the normalized slenderness ratio is lower than 1.5, the effect of joint eccentricity begins to be significant, and as the slenderness ratio decreases, it becomes even more important.

Key Words: Buckling, Brace, Initial imperfection, Cyclic loading, Finite elements

Yüksek Lisans Tezi

ÖZET

UYGULAMA KAYNAKLI BAĞLANTI NOKTASI DIŞMERKEZLİĞİNİN MERKEZİ ÇAPRAZLARIN DAVRANIŞINA ETKİSİ

Necip SANNAH

Karadeniz Teknik Üniversitesi
Fen Bilimleri Enstitüsü
İnşaat Mühendisliği Anabilim Dalı
Danışman: Doç. Dr. Serhat DEMİR
2024, 76 Sayfa

Merkezi çaprazlar birleşim bölgelerinden merkezi yüke maruz kalacağı kabul edilerek tasarlanır. Birleşim bölgelerindeki dışmerkezliği önlemek için, her bir yapısal elemandan aktarılacak iç kuvvetin düğüm noktasından geçmesi gerekmektedir. Ancak, gerçek yapılardaki basınç elemanları tasarım hesaplamalarında varsayıldığı gibi tam olarak düz veya merkezi olarak yüklenmiş değillerdir. Aksine her zaman bir ilkel kusur mevcuttur. AISC 360-22 ve EC 1993'te, merkezi çaprazlardaki ilkel kusurları dikkate almak için belirli güvenlik katsayıları kullanılmaktadır. Ancak, bu güvenlik katsayıları her narinlik oranı için aynıdır ve hangi dışmerkezlik değerine kadar güvenli sonuç verdiği bilinmemektedir. Bu tez kapsamında yukarıda bahsedilen eksikliklere dayanarak, çeşitli uygulama kaynaklı dışmerkezlik durumlarının merkezi çaprazların davranışı üzerindeki etkisini incelemek amacıyla deneysel ve sayısal çalışmalar yürütülmüştür. Çapraz deney elemanları olarak, farklı narinlik oranlarını temsil etmek üzere, aynı kalınlıkta ancak farklı çaplara sahip dört farklı dairesel boş kesit kullanılmıştır. Sonuçlar, uygulama kaynaklı birleşim dışmerkezliğinin merkezi çaprazların burkulma dayanımı üzerindeki etkisinin narinlik oranına bağlı olarak değiştiğini göstermiştir. Deneysel ve sayısal çalışmalara göre, normalleştirilmiş narinlik oranı 1.5'ten büyük olduğunda birleşim dışmerkezliğinin etkisi önemsiz hale gelmeye başlamaktadır. Ancak, normalleştirilmiş narinlik oranı 1.5'ten düşükse, birleşim dışmerkezliğinin etkisi önemli olmaya başlamakta ve narinlik oranı azaldıkça daha da önemli hale gelmektedir. Öte yandan birleşim dışmerkezliği, narinlik oranından bağımsız olarak, burkulma sonrası basınç dayanımının artmasını sağlamaktadır. Bu durum, birleşim dışmerkezliğine sahip çaprazların çekme etkisinde iken düzleşerek dışmerkezlik etkisinin azalmasından kaynaklanmaktadır.

Anahtar Kelimeler: Burkulma, Çapraz, Başlangıç kusuru, Çevrimsel yükleme, Sonlu elemanlar

LIST OF FIGURES

Page No

LIST OF TABLES

Page No

ABBREVIATIONS AND SYMBOLS

λ	: Slenderness ratio
$\bar{\lambda}$	: Non-dimensional slenderness
K	: Effective length factor
L	: Unbraced length of the member
r	: Radius of gyration
f_y	: Characteristic yield strength
A	: Cross-sectional area
A_{eff}	: Effective area
A_g	: Gross area
D	: Diameter
t	: Thickness
ε	: Strain
σ_{max}	: Maximum stress
e_0	: Initial bow imperfection
E	: Elasticity modulus
E_T	: Tangent modulus
ϕ_c	: Safety factor
Pn	: Nominal compressive strength
f_{cr}	: Flexural buckling stress
f_e	: Elastic buckling stress
N_{Ed}	: Design compression force
$N_{b,Rd}$	: Design buckling resistance
χ	: Reduction factor
t_f	: Flange thickness
t_w	: Web thickness
L_B	: Clear length
L	: Full length (pin-pin)
e_t	: Top eccentricity
e_b	: Bottom eccentricity
Δ_y	: Yield displacement

σ_{true}	: True stress
σ_{nom}	: Nominal stress
ε_{true}	: True strain
ε_{nom}	: Nominal strain
U	: Displacement
θ	: Rotation
P_b	: Buckling load
P_{pb1}	: First post-buckling load
P_{pb2}	: Second post-buckling load
P_y	: Yield strength
E_y	: Elastic energy
ε_y	: Yield strain
CBF	: Concentrically braced frames
CCBF	: Conventional concentrically braced frames
DDBD	: Direct displacement-based design
BIE	: Braces with intentional eccentricity
CLB	: Concentrically loaded brace
FIEB	: Frames with intentionally eccentric braces
AISC	: American institute of steel construction
EC	: Eurocode
CFST	: Concrete-filled steel tube
CHS	: Circular hollow section
LPDT	: Linear potentiometric displacement transducer
MPC	: Multi-point constraint
FE	: Finite element
FEA	: Finite element analysis

1. INTRODUCTION

1.1. Introductory Remarks

Concentrically braced frames (CBFs) are the most widely used lateral load resisting systems in steel structures and offer several advantages over other systems. One of the key advantages of CBFs is their ease of design, detailing, and construction. These braces are efficient in providing lateral stiffness, which helps to restrict inter-story drifts and overall lateral deformations during seismic events. The system is relatively straightforward to implement, allowing for efficient and cost-effective construction.

Practical seismic design requirements necessitate allowing buckling and yielding in the diagonal members while preventing inelastic response in other components of the structure (EN 1998-1, 2004). As a result, the cyclic axial response of the diagonal members becomes a critical aspect of the seismic response of a braced frame system. These diagonal members are expected to undergo tension deformations beyond yield and compression deformations into the post-buckling range. Understanding and predicting the behavior of these members under cyclic loading is essential for ensuring the overall performance and safety of the braced frame system during earthquakes.

In practical seismic design, it is crucial to ensure that the diagonal members have sufficient strength and ductility to absorb and dissipate seismic energy while maintaining the overall stability of the structure. Various design approaches, such as capacity design and performance-based design, are employed to achieve this balance between strength and ductility. Overall, the cyclic axial response of diagonal members in concentric braced frames is a critical consideration in seismic design. By understanding and properly accounting for the behavior of these members, engineers can design braced frame structures that effectively resist seismic forces and ensure the safety of occupants and the integrity of the building during earthquakes.

Global slenderness, local slenderness, and initial imperfections are crucial parameters that significantly influence the cyclic behavior of braces in steel structures (Bruneau, 1998; Tremblay, 2002; Elghazouli, 2003; Han et al., 2007). Consequently, modern seismic design provisions have incorporated limits for these parameters to ensure a ductile response under severe earthquake events. While seismic design provisions, such as Eurocode 8 (2004) and

AISC 341-22 (2022), both address the key behavioral aspects of bracing members, they may differ in the specific quantification of important design parameters and the corresponding limiting criteria.

1.1.1. Global Stability

The global slenderness of braces is the most important parameter that significantly influences the overall stability. Braces with lower slenderness ratios generally exhibit higher compressive load-carrying capacities and greater potential for energy dissipation during cyclic loading. On the other hand, as the slenderness ratio decreases, larger deformations occur in the plastic hinge region associated with buckling, resulting in a decrease in ductility. For these reasons, limit values are defined in design codes to ensure the appropriate behavior of the braces.

According to AISC 341-22 (2022), the slenderness ratio λ is defined as:

$$\lambda = \frac{KL}{r} \leq 4\sqrt{\frac{E}{f_y}} \tag{1}$$

where K is the effective length factor, L is the unbraced length of the member, E is the modulus of elasticity (200000 MPa), and r is the radius of gyration (AISC 360-22, 2022). The upper limit for the dimensionless slenderness ratio is stated as 200. This limit is imposed to mitigate the dynamic effects that may occur in very slender braces, as outlined in AISC 341-22.

In European regulations, the dimensionless slenderness ratio for bracing members having Class-1, Class-2 and Class-3 cross-sections is calculated using the formula:

$$\bar{\lambda} = \sqrt{\frac{Af_y}{N_{cr}}} \tag{2}$$

where A is the cross-sectional area, f_y is the characteristic yield strength of the material, and N_{cr} is the critical buckling load. For bracing members with a Class-4 cross-section, the same formula is used, but the effective cross-sectional area, A_{eff}, is used instead of A (Eurocode 3, 2005). The upper limit for the dimensionless slenderness ratio depends on the type of bracing system. For X-braced systems, the upper limit is defined as $1.3 < \bar{\lambda} \leq 2.0$. For single braced systems, the upper limit is specified as $\bar{\lambda} \leq 2.0$. The lower limit of 1.3 for X-braced systems is intended to limit additional loads that may occur in columns before the braces buckle. It's important to note that for structures with up to two stories, there are no slenderness ratio limitations specified (Eurocode 8, 2004).

1.1.2. Local Stability

Global buckling considers the overall stability and strength of compression members as a whole, while local buckling is related to the local stability of individual components that make up the cross-section of the compression member (Aghayere & Vigil, 2020).

After global buckling, a plastic hinge typically forms in the middle region of the brace. This region is highly susceptible to local buckling, where increased compressive forces and longitudinal shortening result in local buckling of the cross-sectional components under compression (Figure 1). With the occurrence of local buckling, deformations concentrate in this region, and the brace fails to reach its full compressive capacity (Aghayere & Vigil, 2020). Additionally, local buckling can lead to premature brace instability and low-cycle fatigue under cyclic loading beyond the elastic range (Goggins et al., 2006). Due to these factors, design codes impose certain limitations on the width-to-thickness ratios of the cross-sectional components that form the compression members.

Figure 1. Local buckling (Demir et al., 2024)

In AISC 360-22, compression members are classified as slender or non-slender based on local buckling. Equation 3 gives the limits for the cross-sectional components of compression members of round hollow structural sections. Braces that meet these limit conditions are classified as non-slender elements.

$$\frac{D}{t} \leq 0.11\frac{E}{f_y} \tag{3}$$

where, *D* represents the diameter, *t* represents the thickness, and *E* represents the modulus of elasticity. Brace members with round hollow structural sections that do not meet these limit conditions are classified as slender elements. Slender elements should be designed according to the conditions specified in AISC 360-22 Section E7, which account for the effects of strength reduction due to local buckling caused by local instability.

In Eurocode 3, compression members are classified into four different classes based on local buckling. The cross-section classification assesses the likelihood of encountering local instability, with a higher class indicating an increased level of risk. The classification is determined based on the strength and ductility capacity of the cross-section. Table 1 provides the necessary conditions for the classification of the cross-sectional components of compression members with round hollow structural sections. Braces that do not meet these limit conditions are considered as Class-4 elements.

Table 1. Maximum width-to-thickness ratios for compression parts (Eurocode 3, 2005)

Round HSS	*Class-1*	$D/t \leq 50\varepsilon^2$	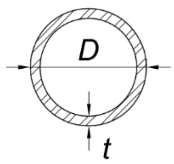
	Class-2	$D/t \leq 70\varepsilon^2$	
	Class-3	$D/t \leq 90\varepsilon^2$	
$\varepsilon = \sqrt{235/f_y}$			

1.1.3. Initial Imperfections

Initial imperfections in steel structures refer to the deviations or irregularities from the ideal geometric and material properties that are assumed during the design process. These imperfections can occur during the fabrication, erection, or service life of the structure. While imperfections are considered undesirable, they are inevitable to some degree and must be accounted for in the design and analysis of steel structures.

When comparing a buckling curve to the theoretical Euler buckling curve, as shown in Figure 2, it becomes apparent that the load-carrying capacity varies depending on the relative slenderness of the brace. The largest difference is observed for braces with intermediate slenderness, where the relative slenderness is approximately 1. This behavior can be attributed to the initial imperfections present in the brace. Members with low relative slenderness are less affected by these imperfections since their load-carrying capacity is primarily governed by yielding rather than buckling. On the other hand, members with very high slenderness experience load-carrying capacity determined by elastic buckling, where the stresses are significantly lower than the yield stress (Yoo et al., 2001; Choi & Yoo, 2005). Consequently, the effect of initial imperfections is not as influential in these cases. The initial imperfections can be categorized as geometrical and material imperfections.

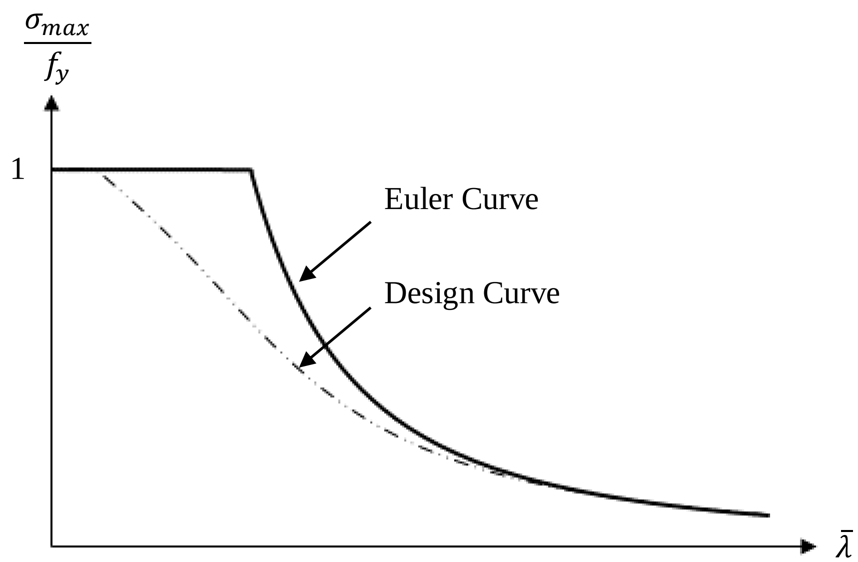

Figure 2. Relationship between design curve and Euler buckling theory

Geometrical Imperfections: These imperfections arise from variations in the dimensions, shape, and alignment of structural members. Examples include variations in member lengths, out-of-plane deformations, variations in member cross-sections, and crookedness of members. Geometric imperfections can affect the overall stability, load distribution, and structural behavior of the steel structure. Steel members inherently possess certain levels of initial crookedness or geometric imperfections, which can result in the generation of second-order moments when subjected to axial compression. These second-order moments have a significant influence on the load-carrying capacity of the member. Furthermore, the magnitude of the second-order moment increases with the degree of initial imperfections. The impact of geometric imperfections can be better understood by examining a pinned-pinned, axially loaded member with an initial bow imperfection, e_0, represented as a half-sine wave, as illustrated in Figure 3. This visual representation helps to illustrate how initial imperfections induce additional moments and subsequently affect the overall response and behavior of the member.

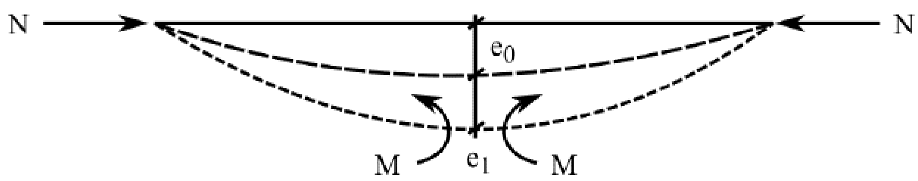

Figure 3. Axially loaded member with an initial bow imperfection, shaped as a half-sine wave, and resultant second order moments

Material Imperfections: During the final stages of the manufacturing process, a structural steel member experiences different rates of cooling, leading to the presence of initial stresses before any loads are applied. These preexisting stresses, known as residual stresses, are caused by the varying cooling rates of different fibers within the steel section. The fibers that cool first are subjected to compressive stresses, while the fibers that cool last experience tension stresses. Residual stresses can also result from processes such as cold bending or straightening, flame cutting, and welding of structural members. Residual stresses in a structural steel section are typically in internal equilibrium and do not affect the plastic moment or tension capacity of the member. However, they do influence the load deformation relationship of the structural element. The impact of residual stresses is particularly significant for axially loaded members like columns and braces, as it causes a reduction in the modulus of elasticity. The modulus of elasticity decreases from the initial elasticity modulus, E, to the tangent modulus, E_T, resulting in a decrease in the Euler buckling load (Aghayere & Vigil, 2020). Parabolic shape stress pattern for an I-cross-section is given in Figure 4.

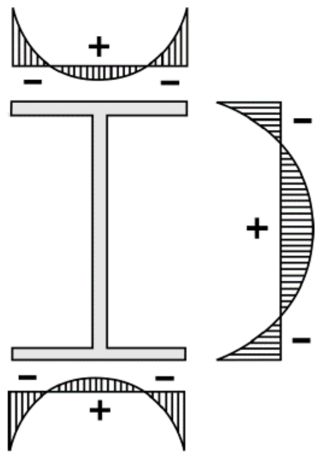

Figure 4. Distribution of residual stresses in a doubly symmetrical cross-section with outstanding flanges (Jönsson & Stan, 2017)

1.2. Buckling Resistance of Braces

Design codes and standards provide guidance on the acceptable levels of imperfections to consider, and appropriate safety factors are applied to account for uncertainties associated with initial imperfections.

To account for initial crookedness, residual stresses, and end restraints in the compression member, the AISC 360-22 (LRFD) specification defines the design compressive strength of an axially loaded member as follows:

$$\phi P_n = \phi_c f_{cr} A_g \tag{4}$$

where ϕ_c=0.90 safety factor, P_n is the nominal compressive strength, f_{cr} is the flexural buckling stress and A_g is the gross cross-sectional area of the axially loaded member. The flexural buckling stress, f_{cr}, is determined as follows:

$$when\ \frac{KL}{r} \leq 4.71\sqrt{\frac{E}{f_y}} \quad \left(or\ when\ f_e \geq\ 0.44 f_y\right)$$

$$f_{cr} = \left[0.658^{\frac{f_y}{f_e}}\right] f_y\ ; \tag{5}$$

$$when\ \ \frac{KL}{r} > 4.71\sqrt{\frac{E}{f_y}}\quad \left(or\ when\ f_e <\ 0.44 f_y\right)$$

$$f_{cr} = 0.877 f_e \tag{6}$$

Equation 5 accounts for the case where inelastic buckling dominates the column behavior because of the presence of residual stresses in the member, while Equation 6 accounts for elastic buckling in long or slender columns.

In EN 1993-1-1 (2005), the determination of the buckling resistance of an axially loaded member is facilitated through a design method that incorporates five buckling curves, as depicted in Figure 5.

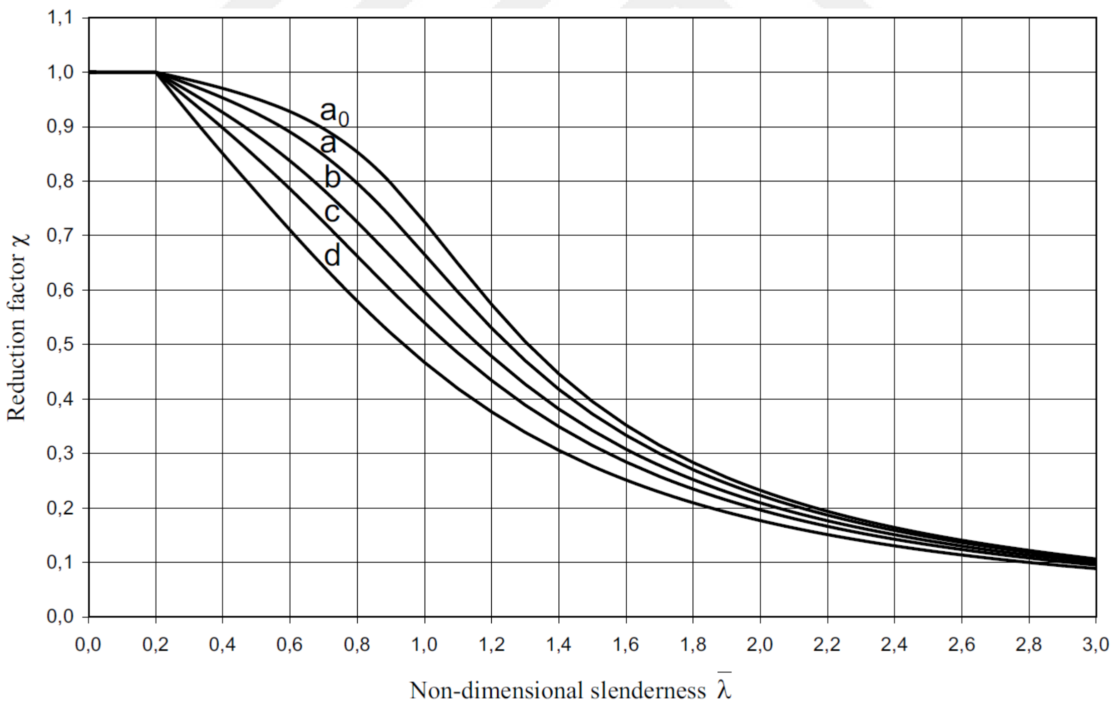

Figure 5. Buckling curves (EN 1993-1-1, 2005)

To ensure the stability of a compressed member, it is necessary to assess the risk of buckling failure by comparing the design compression force, N_{Ed}, with the design buckling resistance, $N_{b,Rd}$ as follows:

$$\frac{N_{Ed}}{N_{b,Rd}} \leq 1.0 \tag{7}$$

The calculation of the buckling resistance for a cross-section with Class 1-3 is determined according to Equation 8. The reduction factor χ can be calculated either analytically using Equation 9 or directly from the buckling curves. The appropriate buckling curve is selected by referring to Table 3. Additionally, the non-dimensional slenderness, $\bar{\lambda}$, can be determined by employing Equation 11 for Class 1, 2 and 3 cross-sections and Equtaion 12 for Class 4 cross-sections.

$$N_{b,Rd} = \frac{\chi A f_y}{\gamma_{M1}} \tag{8}$$

$$\chi = \frac{1}{\Phi + \sqrt{\Phi^2 - \bar{\lambda}^2}} \tag{9}$$

where the factor Φ is determined by:

$$\Phi = 0.5\left[1 + \alpha\left(\bar{\lambda} - 0.2\right) + \bar{\lambda}^2\right] \tag{10}$$

$$\bar{\lambda} = \sqrt{\frac{A f_y}{N_{cr}}} \tag{11}$$

$$\bar{\lambda} = \sqrt{\frac{A_{eff} f_y}{N_{cr}}} \tag{12}$$

The imperfection factor, α, is determined based on the following table extracted from EN 1993-1-1 (2005).

Table 2. Imperfection factors for bucking curves

Buckling Curve	a_0	a	b	c	d
Imperfection factor, α	0.13	0.21	0.34	0.49	0.76

Table 3. Selection of buckling curve for a cross-section (EN 1993-1-1, 2005)

Cross section		Limits		Buckling about axis	Buckling curve	
					S 235 S 275 S 355 S 420	S 460
Rolled Sections	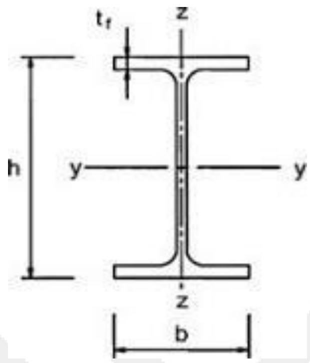	$h/b > 1,2$	$t_f \le 40$ mm	y - y z - z	a b	a_0 a_0
			40 mm $< t_f \le$ 100	y - y z - z	b c	a a
		$h/b \le 1,2$	$t_f \le 100$ mm	y - y z - z	b c	a a
			$t_f > 100$ mm	y - y z - z	d d	c c
Welded I-sections	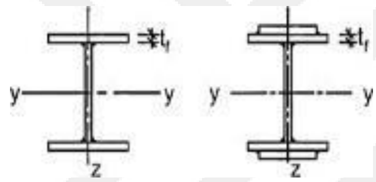	$t_f \le 40$ mm		y - y z - z	b c	b c
		$t_f > 40$ mm		y - y z - z	c d	c d
Hollow Sections		Hot finished		any	a	a_0
		Cold formed		any	c	c
Welded box sections	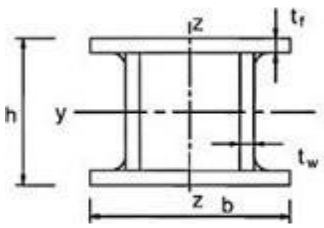	Generally (except as below)		any	b	b
		Thick welds: $a > 0.5\, t_f$ $b/t_f < 30$ $h/t_w < 30$		any	c	c
U-, T- and solid sections	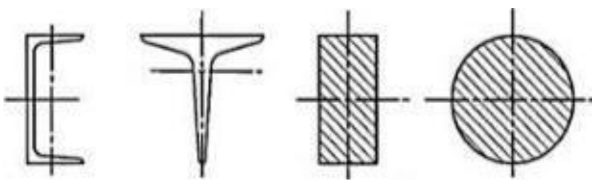			any	c	c
L-sections	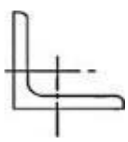			any	b	b

1.3. Research Significance and Scope

CBFs is typically formed by a system of structural members joined together at their ends to form a stable framework. Concentric braces are designed based on the assumption that they have concentrically loaded joints. To avoid eccentricity at a joint, the line of action of the load from each member framing into a joint should intersect at the joint centroid (Figure 6-a). However, compression members in real structures are not perfectly straight (sweep, camber), perfectly aligned, or concentrically loaded as is assumed in design calculations; there is always an initial imperfection (Yoo & Lee, 2011; Klasson et al., 2016; Madah & Amir, 2018). One particular effect is the introduction of load eccentricity, which can cause a fundamental change in the distribution of stresses and strains compared to a structure subjected to uniform compression. This altered state of loading can lead to a significant decrease in the buckling resistance and result in the structure operating in a post-buckling regime. When a braced structure prematurely enters a buckling state, it can experience a significant reduction in its strength properties and lead to the accelerated failure of load-carrying members (Debski & Teter, 2019). Therefore, many design situations require the evaluation of joint eccentricity.

Some examples of these accidental joint eccentricities are illustrated in Figure 6. The application that the brace centerline intersect the beam-column joint just like the analysis model is represented in Figure 6-a. Figure 6-b illustrates that the centerline of the brace do not intersect the beam-column joint. As a result, unintentional load eccentricity is introduced due to factors such as fabrication tolerances, member straightness, or the connection method. On the other hand, in some practical connections, eccentricities are intentionally introduced to reduce the amount of gusset plates and improve workability (Kim, 2001), even if the connection is concentric in the analysis model. (Figure 6-c).

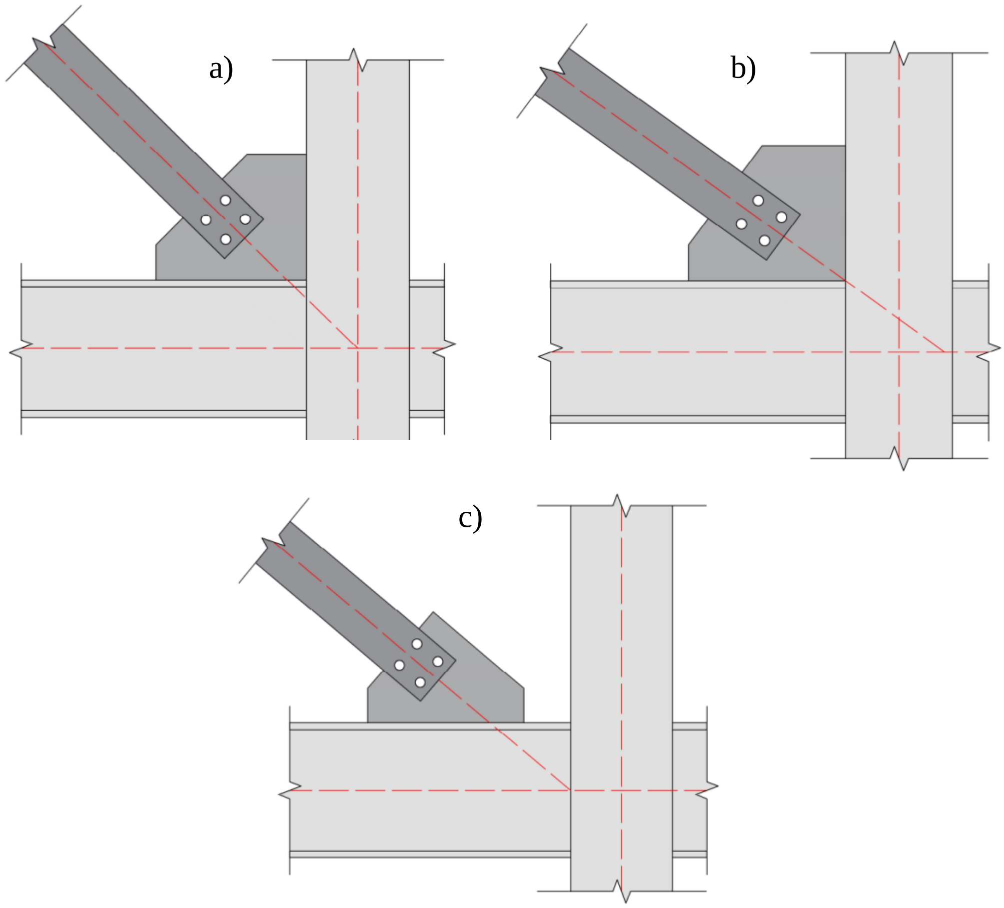

Figure 6. Accidental joint eccentricity examples

In order to restrict geometrical imperfections, certain tolerances have been defined in ANSI/AISC 303-22 (2022) and EN 1090-2 (2018). Structural steel frame tolerances given in these standards refer to the acceptable deviations or variations in dimensions, alignments, and other parameters of steel structural members within a steel frame construction. These tolerances are specified to ensure that the overall structure meets the required design criteria and functional requirements. ANSI/AISC 303-22 (2022) and EN 1090-2 (2018) define specific tolerances like members' length, verticality of columns, level of slabs, diameter of holes etc. However, these standards do not offer any guidance to the engineer and fabricator in the establishment of reasonable alignment tolerances for brace members.

In AISC 360-22 and EC 1993, certain safety factors applied to consider uncertainties related to initial imperfections of concentric braces. However, these safety factors are the same for each slenderness ratio, and it is not known up to which eccentricity level they provide a safe result. Based on these shortcomings, an experimental program was carried out at the Structural and Material Laboratory of Karadeniz Technical University. Four sets of specimens, totaling twelve steel brace specimens, were designed to examine the effect of various accidental joint eccentricity conditions on the behavior of concentric braces. For the brace specimens, four different circular hollow sections with the same thickness but different diameters were used to represent a range of global slenderness.

1.4. Objectives

In summary the objectives of this study are to:

i. Investigate the cyclic behavior of steel braces under low eccentric loading, for better understanding and representation of their buckling strength, failure modes and post buckling behavior, for design and evaluation purposes.
ii. Compare the buckling strength of the tested brace specimens with existing design codes.
iii. Determine the allowable tolerances for load eccentricities in concentric braces.

1.5. Literature Review

Debski and Teter (2019) conducted a study on short thin-walled Z-columns made of carbon-epoxy laminate under eccentric compressive load. Both experimental tests and numerical simulations were conducted to analyze buckling and post-buckling behavior. Experimental results were utilized to confirm the accuracy of the numerical models in the study. The study examined the influence of load eccentricity on buckling load and rigidity in the post-buckling state. Results indicated strong agreement between experimental and numerical findings, providing valuable insights into the quantitative impact of load eccentricity on the structure. The vertical tangent and P-εm intersection methods provided similar, but significantly overestimated, bifurcation load values. Although there was no quantitative agreement, the study demonstrated a qualitative agreement: an increase in load eccentricity consistently led to a decrease in the buckling load determined by all methods.

A study conducted by Zhao et al. (2014) focused on investigating the mid-height horizontal bracing forces of column-bracing systems with pin-ended and fixed-ended column bases, by implementing random geometric imperfections combinations on a large number of finite element models. It was found by the study that column-bracing systems with pin-ended column bases have higher ultimate load-carrying capacity and mid-height horizontal bracing forces compared to those with fixed-ended column bases. Random geometric imperfections led to the variability of bracing forces in compression or tension, allowing for reasonable reductions in design bracing forces. The paper proposes practical design formulas for mid-height horizontal bracing forces.

Ureña et al. (2021) carried out a study on Frames with Intentionally Eccentric Braces (FIEBs) as an alternative to conventional Concentrically Braced Frames (CBFs) in seismic design. The objective was to assess the seismic performance and cost-effectiveness of FIEBs using a Direct Displacement-Based Design (DDBD) method. Buildings with 4, 8, and 12 stories were designed with HSS brace members, targeting drift ratios of 1.5% and 2.5%. Non-Linear Response-History Analysis was performed to evaluate the buildings' performance. The results indicated that the design procedure was suitable for FIEBs, demonstrating satisfactory seismic performance and compliance with performance objectives. FIEBs were found to be economically advantageous compared to conventional CBFs.

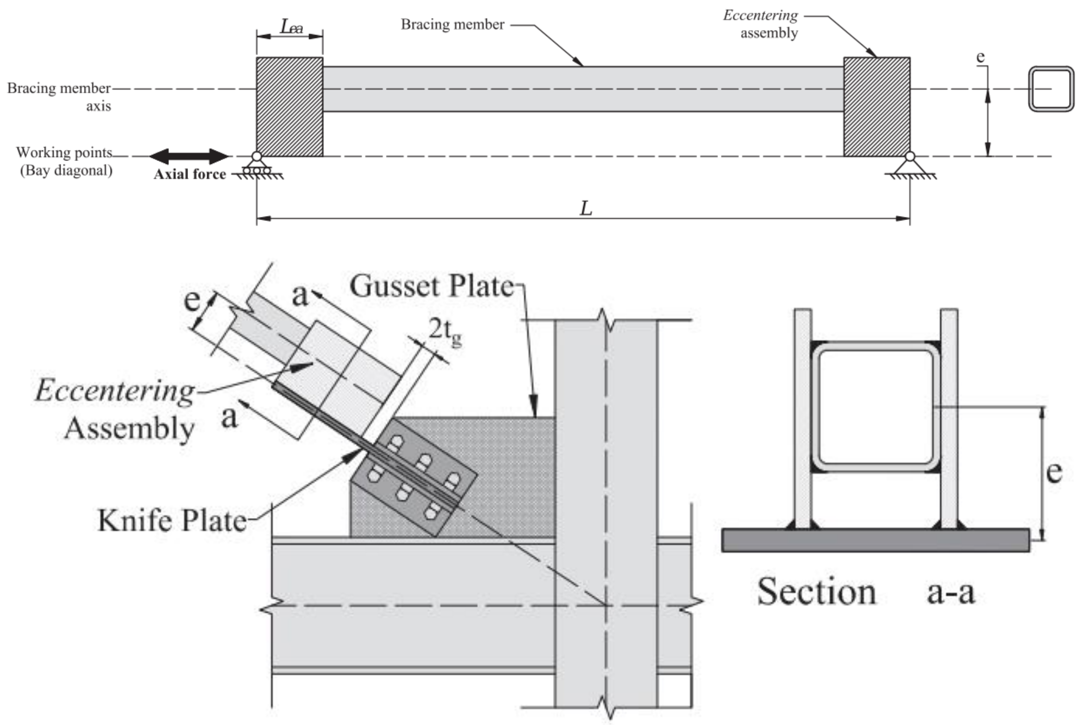

Figure 7. The eccentricity assembly considered in Ureña et al.'s (2021) study

Ureña et al. (2022) also conducted a study with the objective of investigating the performance of Braces with Intentional Eccentricity (BIEs) as an alternative to Concentrically Loaded Braces (CLBs). Four full-scale square ASTM A1085 HSS BIE specimens were tested under reversed cyclic loading. The specimens were designed to comply with or exceed slenderness limits. Experimental and numerical results exhibit the benefits of introducing eccentricity in BIEs. However, it was observed that the failure mode in BIEs, which are more resistant to mid-length local buckling, can be governed by fracture at the bracing member's ends due to rotational demand. The implications of these findings on the design of Frames with Intentionally Eccentric Braces (FIEBs) are discussed.

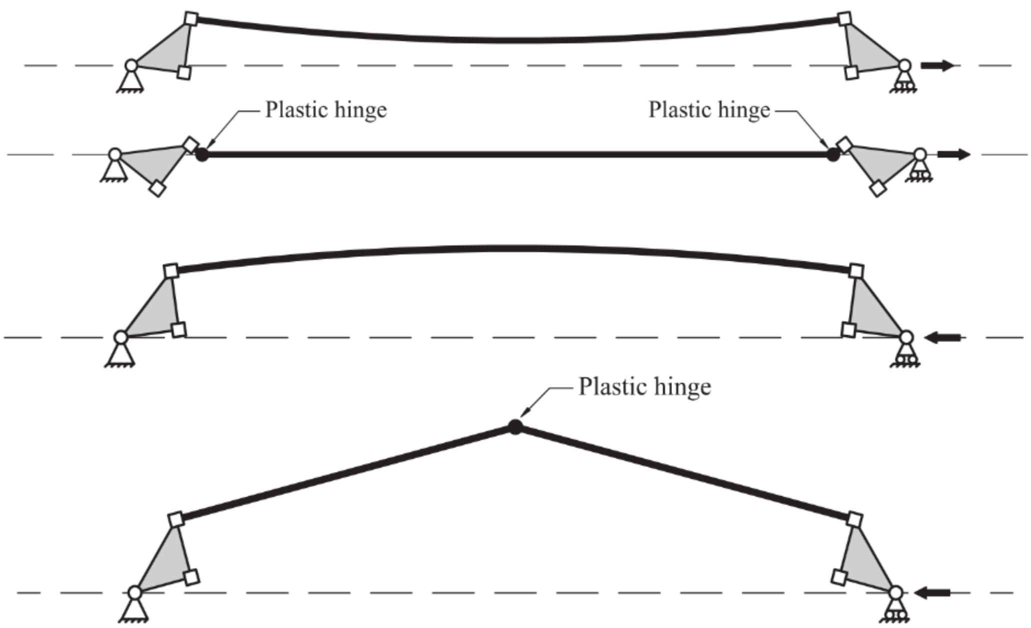

Figure 8. Deformed shape of BIE under tension and compression (Ureña et al., 2022)

Wang et al. (2019) conducted a study on the degradation of buckling stability in circular steel tubes with bolt-ball joints under installation eccentricity. Eccentric compression tests were performed on various joint specifications and installation eccentricities, obtaining the degradation characteristics of buckling stability. Detailed finite element models with bolt threads were established using Ansys (2016), and good agreement between simulation and test results was confirmed, validating the numerical simulation method. Subsequently, eighteen simulation schemes were carried out to analyze tube buckling behavior under different eccentricities. The results indicated an approximately linear decrease in stability capacity with installation eccentricity consistently with the experimental findings and a slight drop in the decrease speed as the eccentricity increases.

A reduction factor was proposed for considering stability capacity reduction in engineering design when dealing with different eccentricities in circular steel tubes with bolt-ball joints.

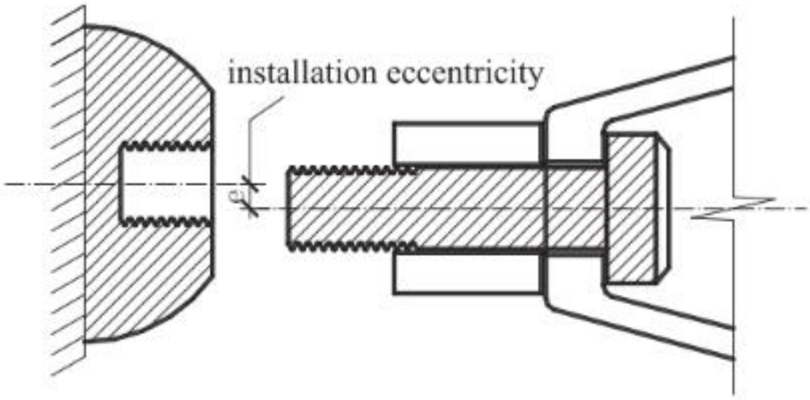

Figure 9. Installation eccentricity (Wang et al., 2019)

Wang et al. (2021) conducted a study on low-ductility concentrically braced frames (CBFs) in low to moderate seismic regions that are referred to as Conventional CBFs. Their objective was to analyze the inelastic behavior of brace connections in CCBFs. A high-fidelity finite element simulation method was developed and validated. The study revealed nonuniform shear distribution within the bolt group and quantified the impact of loading eccentricity on the weld group. Recommendations were provided to prevent bolt shear rupture and premature weld fracture.

In another study, Hernández-Figueirido et al. (2012) investigated the behavior of rectangular and square tubular columns filled with normal and high strength concrete. The columns were subjected to non-constant bending moment distributions by altering the top and bottom eccentricities. The results showed that high strength concrete was advantageous for non-constant bending moments, while normal strength concrete provided improved ductility. However, the comparison of the ultimate load for each test with the design loads from Eurocode 4 (2004) unsafe results falling within a 10% safety margin.

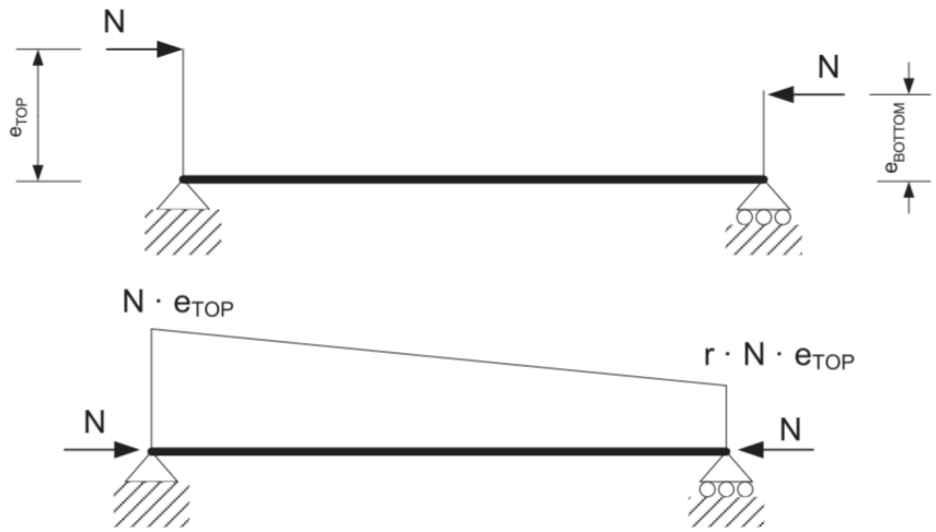

Figure 10. Non-constant bending moment from Eurocode 4 (Hernández-Figueirido et al., 2012)

Harvey Jr. and Cain (2020) investigate the imperfections in buckling analyses, considering initial member imperfections and load eccentricity together rather than separately. The focus was on the scenario where these two effects cancel each other out. A linear analysis was conducted to determine the critical ratio of load eccentricity to member imperfection amplitude, which leads to a change in the column's buckling direction. Experimental tests were carried out to validate the findings, utilizing 3D-printing to incorporate predefined geometric imperfections.

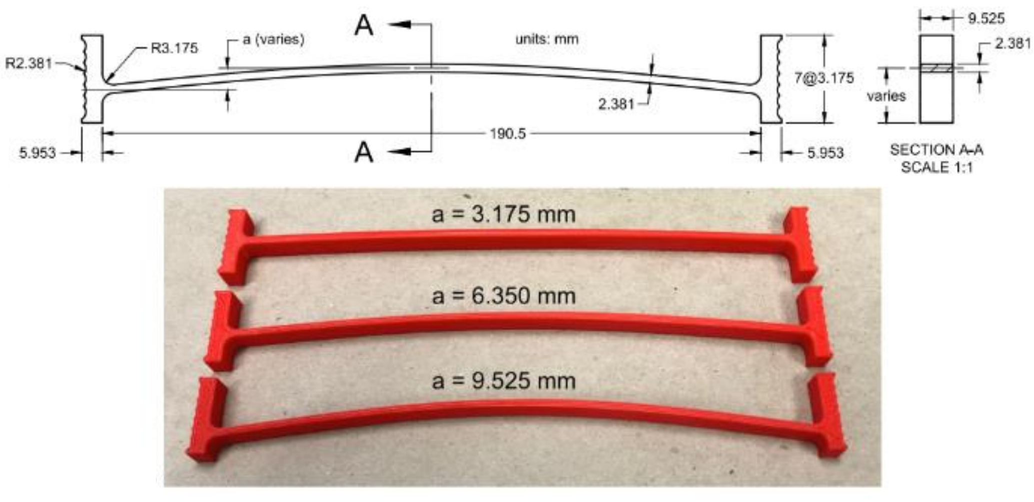

Figure 11. Debski and Teter’s (2019) test specimens

Albero et al. (2022) conducted experimental tests on circular concrete-filled steel tubular (CFST) beam-columns loaded under unequal eccentricities at both ends. The behavior of CFST columns under this loading scheme, which is common in multi-story frames, was assessed. It was revealed by the test results that the ultimate resisting load is increased when the column is loaded under unequal eccentricities compared to what is loaded under equal eccentricities. The equivalent moment factors provided by Eurocode 4 and AISC 360–22 were evaluated in the study, and it was found that both codes offer safe predictions for higher slenderness beam-columns but provide unsafe predictions for double curvature members with low slenderness. It has been observed that there is a requirement for further research in order to enhance the moment factor proposals.

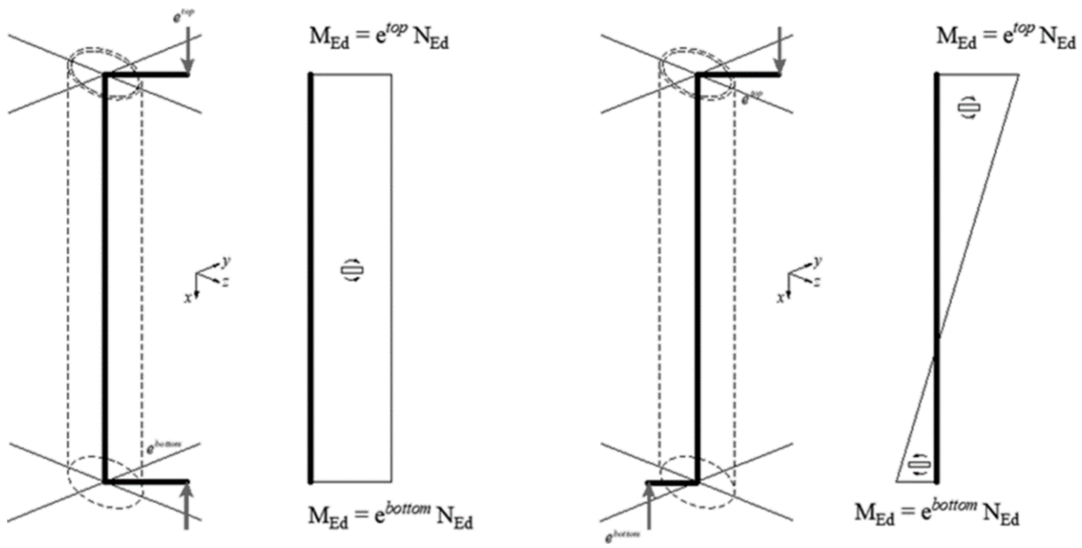

Figure 12. Load eccentricity at ends (Albero et al., 2022)

Saidani (1998) conducted a study on the impact of joint eccentricity on the local and overall behavior of the of truss girders made from rectangular hollow section members, which involved analyzing three truss girders with varying joint eccentricities using numerical models The author investigates the influence of eccentricity on the elastic distribution of axial forces and moments. To ensure an accurate representation of the tested girder, evaluations are conducted by comparing it to a prototype lattice girder and a finite element simulation of the joints and members. The results showed that connection eccentricity significantly affects the axial force distribution in bracings, leading to significant changes in bending moments, while truss deflection remains minimally affected.

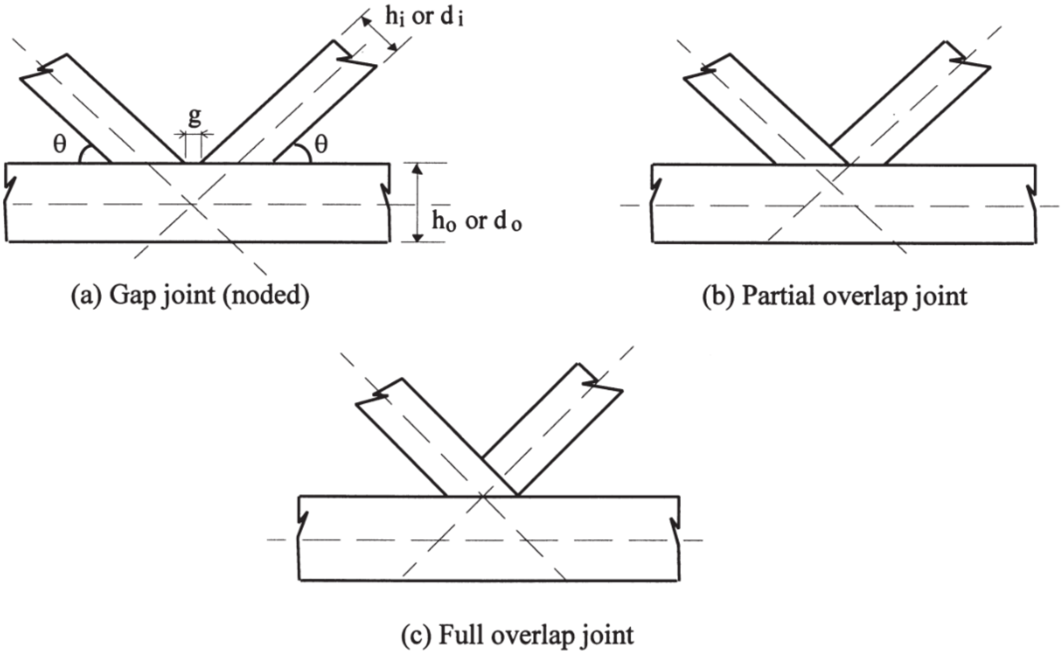

Figure 13. Type of joints with eccentricities (Saidani, 1998)

A study performed by Çayır et al. (2022) aimed to investigate the behavior of steel elements with different geometric properties under axial compressive forces and determine the effects of initial imperfections and residual stresses. Finite element models were used to perform the analyses. The results showed that in some cases, the critical buckling stresses were lower than the values recommended in the regulations. The authors indicated that the values of initial imperfections need to be further examined and supported by experiments. The obtained results demonstrated that both the initial imperfections and residual stresses influenced the behavior of steel elements. Consequently, further research in this area was recommended.

2. EXPERIMENTAL PROGRAM

This chapter presents the design and specifications of brace specimens, as well as test setup and instrumentation used in the experimental program.

2.1. Design and Specifications of Brace Specimens

Four sets of specimens, with a total of twelve steel brace specimens were designed to investigate the effect of different accidental eccentricity conditions on the behavior of the concentric braces. As brace specimens, four different circular hollow sections (CHS) having same thickness but different diameters (76.1x2, 60.3x2, 48.3x2 and 42.4x2 mm) were employed to represent a range of global slenderness. Normalized global slenderness ratios of the specimens varied from 0.92 to 1.68 and conform to the requirements of EC3 and AISC 360-22. All cross sections are deemed as Class-1 or non-slender sections according to EC3 and AISC 360-22, respectively, and comply with the requirements of Ductile Braced Frames. Complete information on the specimen configuration and details of specimens are given in Figure 14 and Table 4.

For all specimens the clear length of brace (between base plates), L_B, and the full length between hinge points (pin to pin), L, are 1570 and 2260 mm, respectively. Brace specimens were welded to base plates with E42 type electrode from both ends. Stiffeners were used to provide an adequate length of weld for the transfer of force between the brace and the base plates. Brace specimens produced for the cyclic loading test are given in Figure 15.

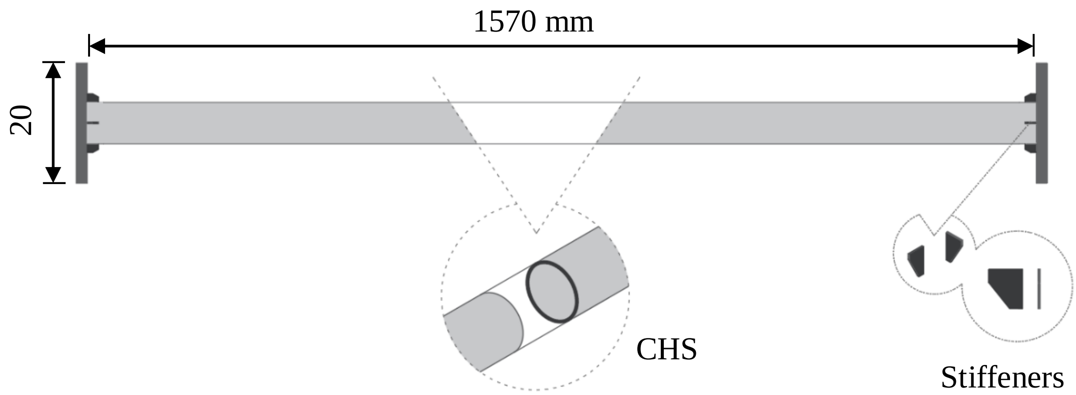

Figure 14. Configuration of the test specimens

Table 4. Details of the test specimens

Test Specimen	**Diameter *d*, (mm)**	**Thickness *t*, (mm)**	**Clear Length L_B, (mm)**	**Pin to Pin Length *L*, (mm)**	**Top eccentricity $e_{t,x}$, (mm)**	**Bottom eccentricity $e_{b,x}$, (mm)**	**Local Slenderness**		**Global Slenderness**	
							EC3	**AISC**	**EC3**	**AISC**
							***d/t* $(50.0)^a$**	***d/t* $(93.6)^b$**	**$\bar{\lambda}$ $(2.0)^b$**	**λ $(200)^b$**
42A					0	0				
42B	42.4	2	1570	2260	+9.65	+9.65	21.2		1.68	158.39
42C					+9.65	-9.65				
48A					0	0				
48B	48.3	2	1570	2260	+11.1	+11.1	24.15		1.47	138.10
48C					+11.1	-11.1				
60A					0	0				
60B	60.3	2	1570	2260	+14.1	+14.1	30.15		1.17	109.95
60C					+14.1	-14.1				
76A					0	0				
76B	76.1	2	1570	2260	+18.1	+18.1	38.05		0.92	86.45
76C					+18.1	-18.1				

^{a}: Upper limit for Class-1, ^{b}: Upper limit in related code

Figure 15. Produced test specimen

As it's seen in Table 4, each set of specimens included three braces having same cross section but different eccentricity conditions. Condition A represents centric loading (no eccentricity), condition B represents positive eccentricity at both ends (equal eccentricity) of the brace specimen, and condition C represents positive eccentricity on the top while negative on the bottom ends (unequal eccentricity) of the brace specimens (Figure 16). The specimens are identified according to section diameter (42, 48, 60, 76) and eccentricity condition (A, B, C), e.g., 48A represents the specimen having 48.3x2 mm CHS and eccentricity condition A.

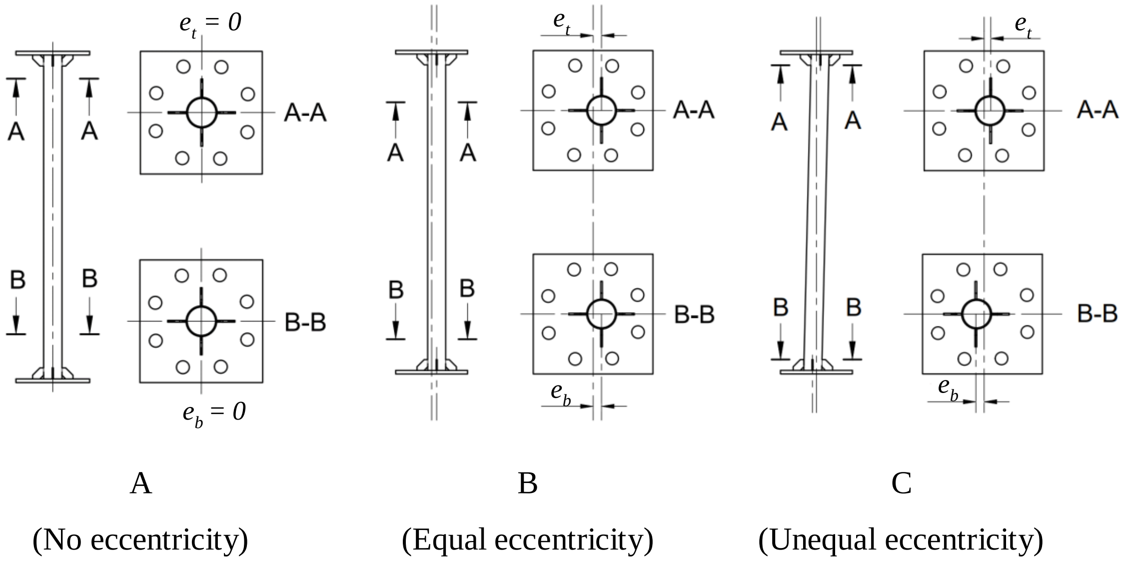

Figure 16. Eccentricity conditions A- no ecc. B- one-side offset C- opposite offset

2.1.1. Determination of Accidental Eccentricities

To simulate accidental joint eccentricity that could occur due to fabrication and construction inaccuracies, specific eccentricities were applied in the laboratory tests on brace specimens. Eccentricities which could be accidentally introduced were assumed to be very low, thus, the whole cross section remains under compression forces. To do this, the magnitudes of the accidental eccentricities were determined with the sectional core area theory, also known as the cross-section kern. This theory states that there exists a limited area within a cross section where no fiber is in tension when a compression force is applied inside this area (Guardiola Víllora, 2019). Figure 17 demonstrates the sectional core area for CHS, and magnitude of eccentricities for different diameters to be used in the experimental studies. Eccentric loadings are applied at the edge of sectional core area at positive or negative sides (depending on the top or bottom of the brace) of *x* axis (marked as red or green). Determined values of *e* did not exceed *0.25d*. If *e* is greater than *0.25d*, it is necessary to take the effect of bending moment of the brace on the load-bearing capacities of joints into account (EC3).

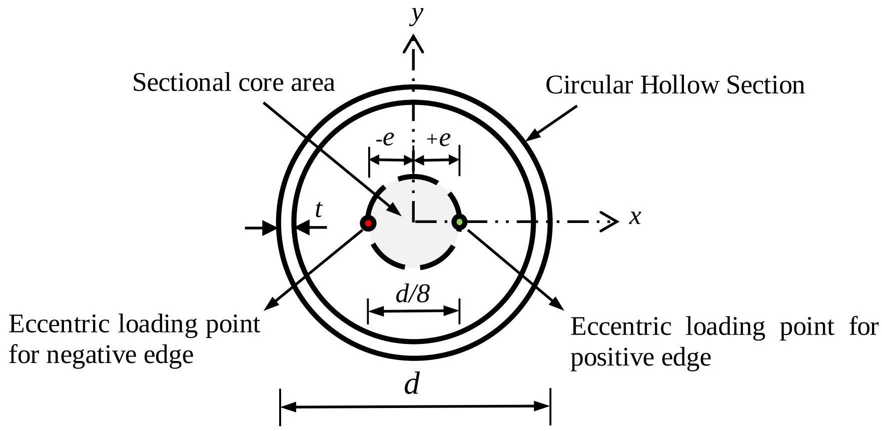

Diameter ***d (mm)***	**Thickness** ***t (mm)***	**Eccentricity** **+/- *e (mm)***
76.1	2	18.1
60.3	2	14.1
48.3	2	11.1
42.1	2	9.65

Figure 17. Sectional core area of CHS and determined eccentricities

2.2. Material Properties

The CHS used in the study were manufactured by the producer through cold forming of carbon steel sheets. The actual mechanical properties of the brace specimens were determined via uniaxial tensile test. For ease of fabrication, short CHS specimens were used instead of tensile coupons. Three short tensile test specimens for each CHS cut from the same lengths of steel used to fabricate brace specimens were prepared in accordance with TS EN ISO 377 (2017) and uniaxial tensile tests were conducted in accordance with EN ISO 6892-1 (2016). The overall length of the short tensile test specimen is 280 mm (Figure 18). Stiffeners are placed to provide an adequate length of weld for the transfer of force between specimen and base plates.

General view of fabricated short tensile test specimens before, during and after uniaxial test are given in Figure 19. Figure 20 illustrates the step by step tensile test, which involves gross section necking, followed by fracture. Mean mechanical properties of short tensile test specimens are summarized in Table 5.

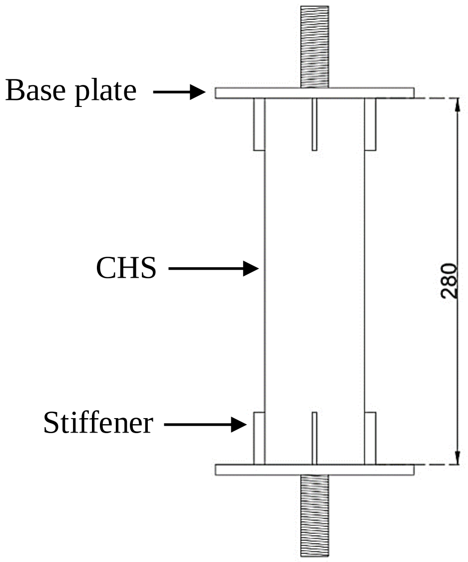

Figure 18. Geometric properties of the short tensile test

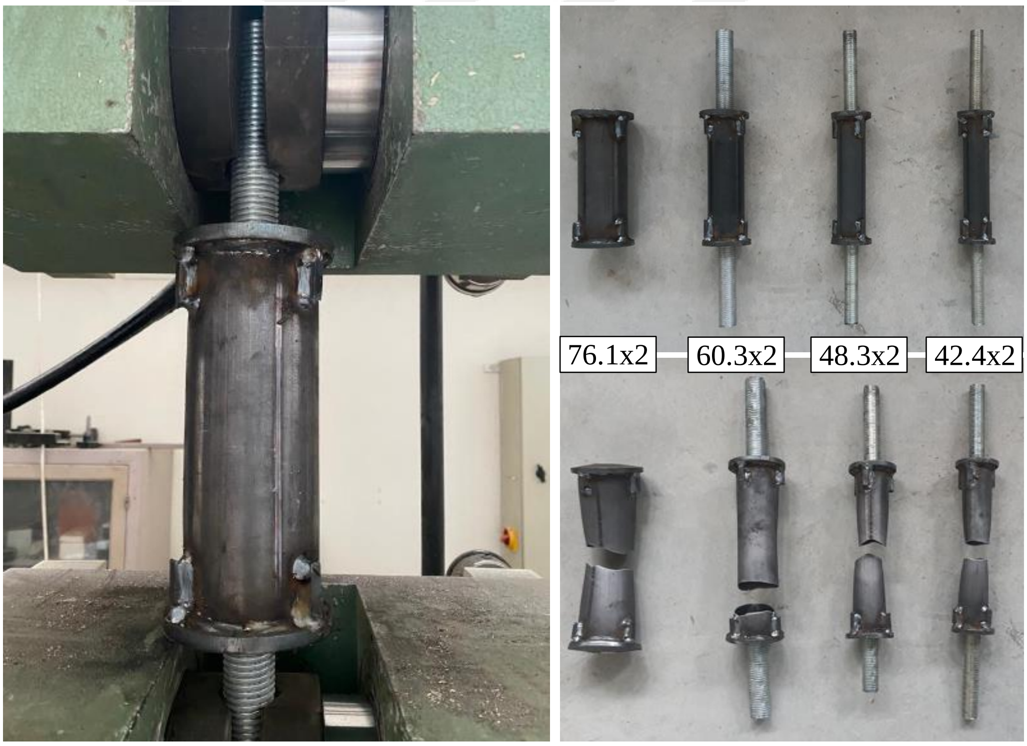

Figure 19. Uniaxial tensile test on short specimens

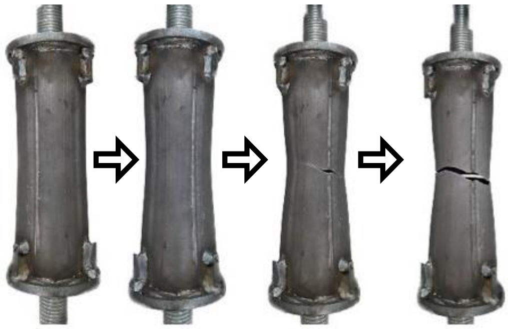

Figure 20. Gross section necking and fracture of a short tensile test specimen

Table 5. Mean mechanical properties of short tensile test specimens

Specimen Diameter	**Thickness *(mm)***	**Length *(mm)***	**Yield Strength *(MPa)***	**Tensile Strength *(MPa)***	**Rupture Elongation *(%)***
76.1	2	280	291.9	386.5	18.3
60.3			340.6	406.4	18.2
48.3			274.9	363.7	21.2
42.4			380.0	440.8	14.7

2.3. Test Setup and Instrumentation

The experimental studies on the brace specimens were conducted at the Structural and Materials Laboratory of the Department of Civil Engineering at Karadeniz Technical University. The test setup was designed to simulate the end connections, deformations, and loadings expected in a concentrically braced frame, as shown in Figure 21.

The HEB200 columns in the test setup have been connected at the top to a stiff beam, while the bottoms of the columns are securely anchored to the stiff floor. This configuration forms a closed-loop system. A 280 kN Dartec servo-hydraulic actuator, vertically fixed to a stiff beam, was used to apply the load. The load was resisted in the test frame by the stiff beam at the back of the actuator and the stiff floor at the opposite end of the specimen. Brace specimens were placed in the test setup, and pinned end connections were provided, as depicted in Figure 22. This rotation-free boundary condition corresponds to a theoretical effective length factor of $K=1.0$.

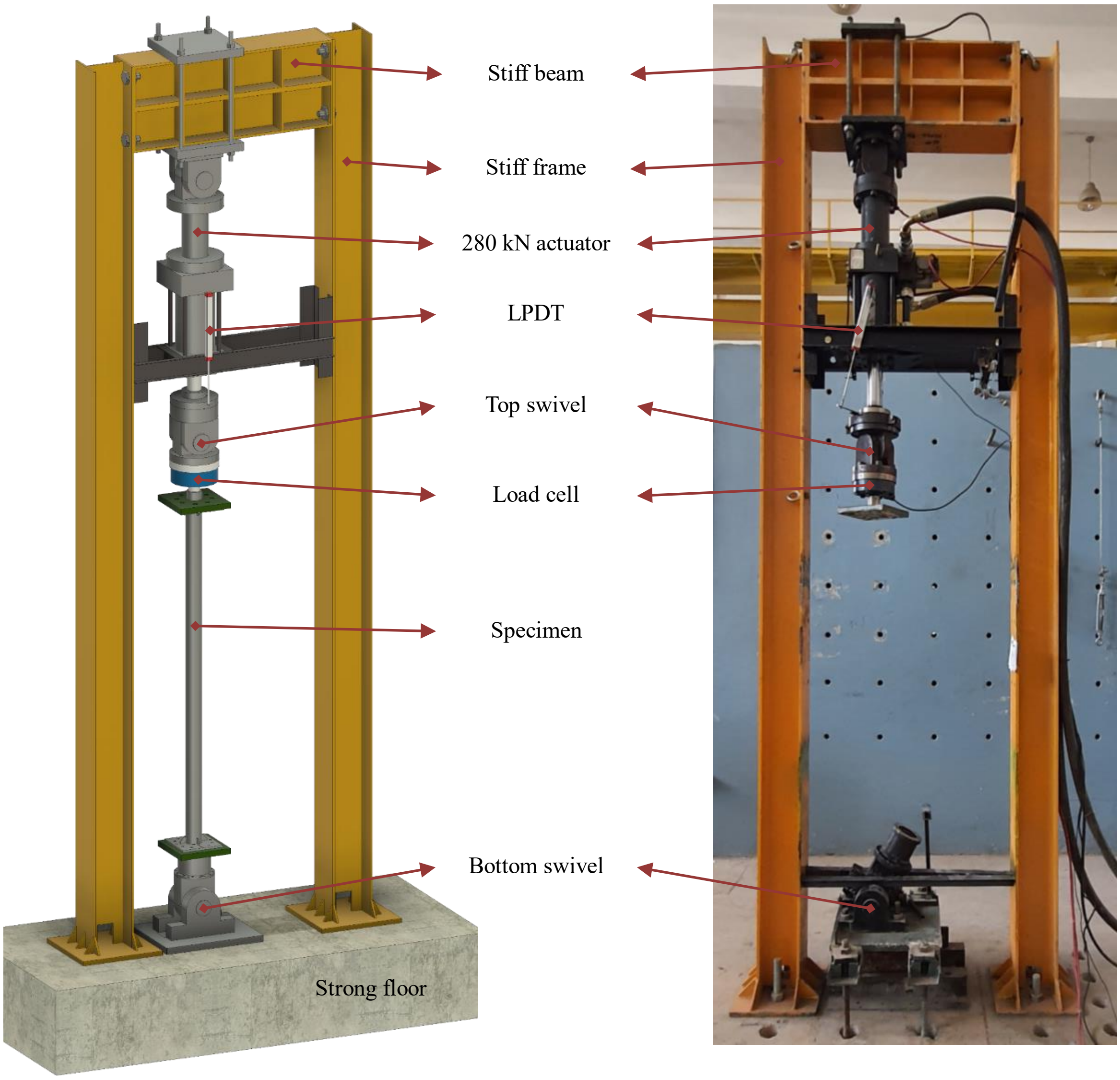

Figure 21. Test setup

Throughout the experiments, measurements of axial load and axial displacements were taken. Axial load was measured using a 500 kN capacity load cell positioned between the brace specimen and the actuator, while axial displacement was measured with a ±100 mm capacity displacement transducer (LPDT). All measurements were recorded using a TDG Coda AI8b data logger.

Figure 22. Specimen 76A ready for test

2.4. Loading Protocol

All brace specimens were tested under displacement controlled quasi-static cyclic loading. The loading history has been found to be a critical factor affecting the performance of members under cyclic axial loading (Elchalakani et.al. 2003). The cyclic axial displacement history was applied according to the recommendations of ECCS (1986), i.e., one cycle at each level of *0.25*, *0.5*, *0.75* and $1.0\Delta_y$ followed by three repeated cycles at each level of *2.0*, *4.0*, *6.0*, *8.0*, *10.0*, *12.0* and $14.0\Delta_y$, where Δ_y is the yield displacement estimated depending on the clear length, L_B, and the yield strain at the 0.2% proof stress. A typical loading history is given in Figure 23. All specimens were subjected to compressive loads first and followed by tensile loading. The displacement was applied with a strain rate of $3x10^{-4}$ s^{-1} to exclude the dynamic effects BS 7270 (2006) and continuously increased until the failure.

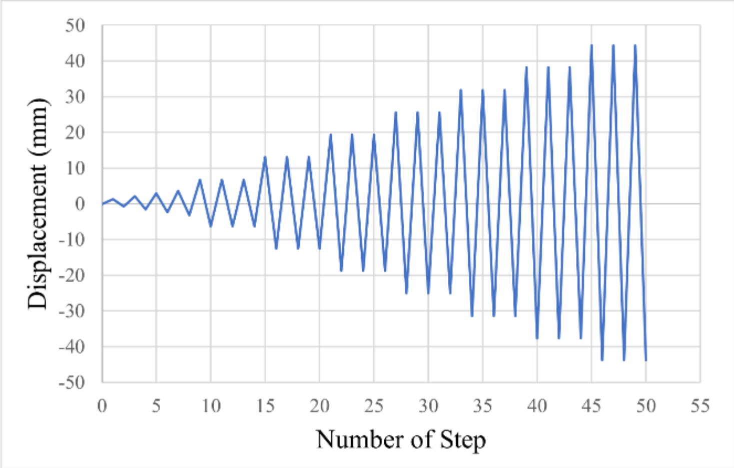

Figure 23. Loading protocol

3. NUMERICAL PROGRAM

This chapter presents the nonlinear finite element analyses performed using the Ansys (2016) software to explain the buckling strength, post-buckling strength, and behavior of damage accumulation in steel brace specimens under cyclic loading. The analyses utilized three-dimensional modelling techniques that consider the interaction between components and account for geometric and material nonlinearity criteria.

3.1. Element Type

The brace specimens were modelled using four-nodal structural shell finite elements (Shell181) (Figure 24). These elements have six degrees of freedom per node, including three translational and three rotational. The modelling approach includes a reduced integration formulation, with one integration point in the planar view and three integration points through the element thickness. The hourglass control feature is also incorporated. The stiffness of these finite elements is composed of both membrane and bending components, following the Mindlin-Reissner theory, which accounts for linear transverse shear deformation effects. Shell181 is used for analyzing thin to moderately thick shell structures. It supports linear, large rotation, and large strain nonlinear applications, accounting for changes in shell thickness (Ansys, 2016).

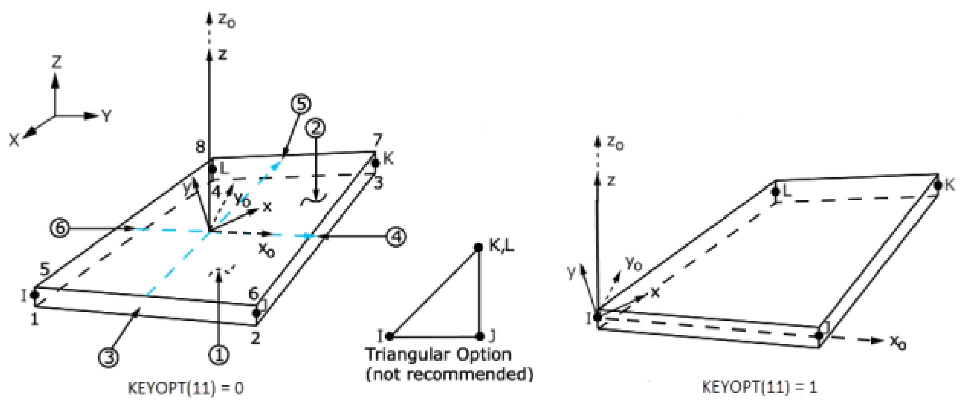

Figure 24. Shell181 element (Ansys, 2016)

3.2. Material Model

The material model used in the finite element analysis considered the strain hardening characteristic of steel by employing the multilinear kinematic hardening plasticity model which is recommended for steel and similar materials. The mean mechanical properties of the steel used in the production of the brace specimens were determined through tensile tests as explained in Chapter 2. In order to use the mean stress-strain curve obtained from short tensile test specimens in finite element analyses, it is necessary to convert these curves into true stress-true strain curves. The experimental (nominal) stress-strain curve is converted into the logarithmic (true) stress-true strain curve (Figure 25) using Equations 13 and 14, as these are required for geometrically nonlinear analysis purposes. The Poisson's ratio for the steel material is assumed to be 0.3.

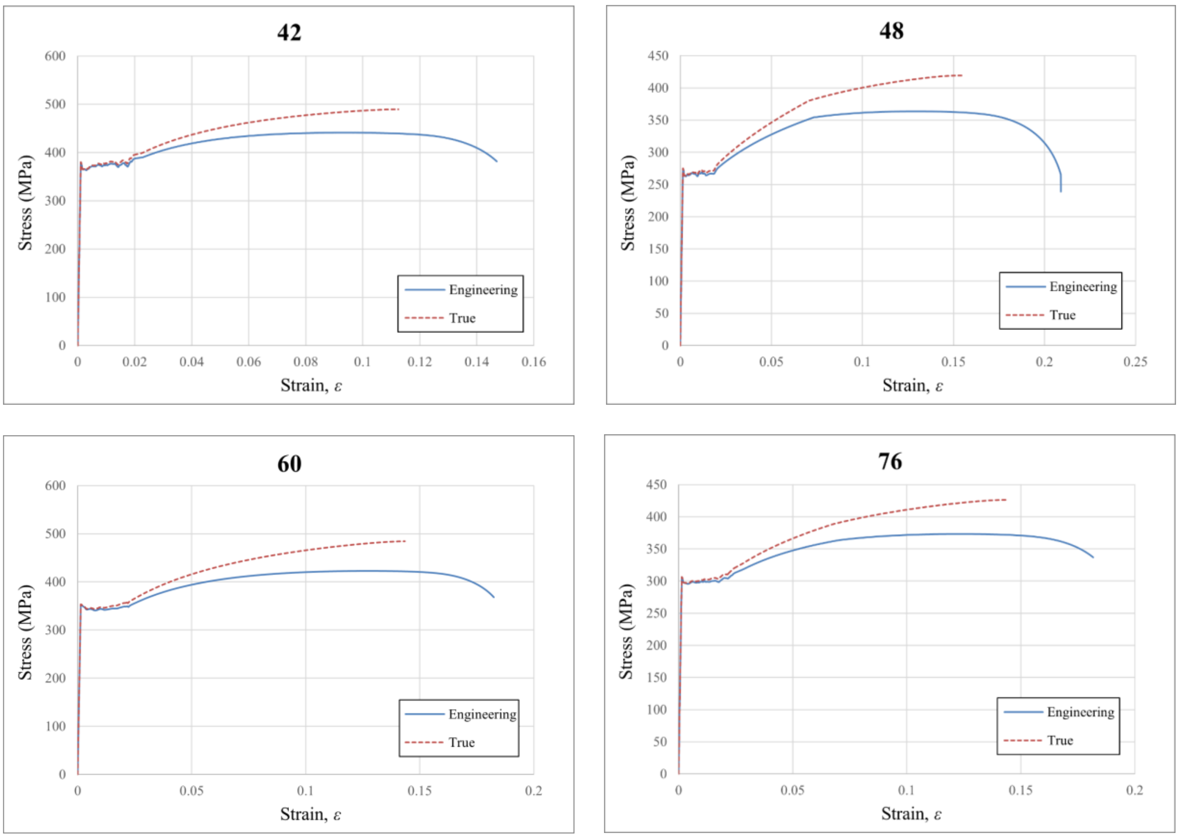

Figure 25. True stress-strain graphs of tensile test specimens

$$\sigma_{true} = \sigma_{nom}.(1 + \varepsilon_{nom}) \tag{13}$$

$$\varepsilon_{true} = \ln(1 + \varepsilon_{nom}) \tag{14}$$

During the process of sectioning, the material strips that are released may display curvature and axial deformation, indicating the presence of bending (through-thickness) and membrane residual stresses, respectively. Typically, cold-formed sections are characterized by dominant bending residual stresses (Cruise & Gardner, 2008). In this study bending residual stresses were inherently incorporated into the material properties to a significant extent by utilizing short tensile test specimens extracted from the CHS (Section 2.2).

3.3. Mesh Sensitivity Analysis

To ensure the accurate convergence of solutions, a study on mesh convergence was carried out due to the sensitivity of strain outputs to the mesh size. In order to achieve this, displacement-controlled monotonic compression analyses were performed on three different finite element models. These models were created with mesh sizes of 5 mm, 10 mm, and 15 mm, as illustrated in Figure 26. The obtained results of reaction forces are compared in Figure 27, while the principal strain outputs of a selected node from the buckling region of the models are compared in Figure 28.

While the reaction forces in Figure 27 demonstrate quite similar results, Figure 28 reveals that noteworthy variations in principal strains emerge as displacements increase. It is observed that mesh sizes 5 and 10 mm exhibit less variation compared to 15 mm, and as the element size decreases, the significance of the variation diminishes. Based on these findings, it has been decided that meshing all the models using quadrilateral elements with a size of 10 mm would be sufficient. The aspect ratios of the finite elements are 1 in both the longitudinal and transverse directions. The mesh configuration for all sections of the models was kept identical, with special attention given to maintaining the orthogonality of the arrangement. Additionally, 5 integration points have been used along the thickness of the Shell181 element.

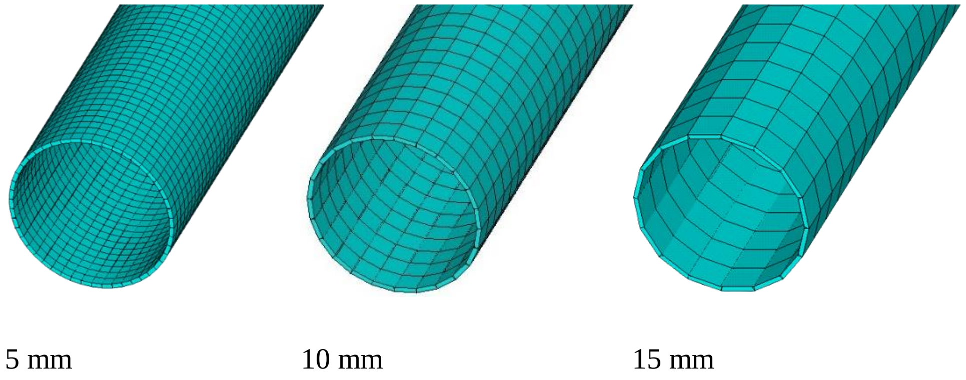

Figure 26. Mesh sizes of the sensitivity study

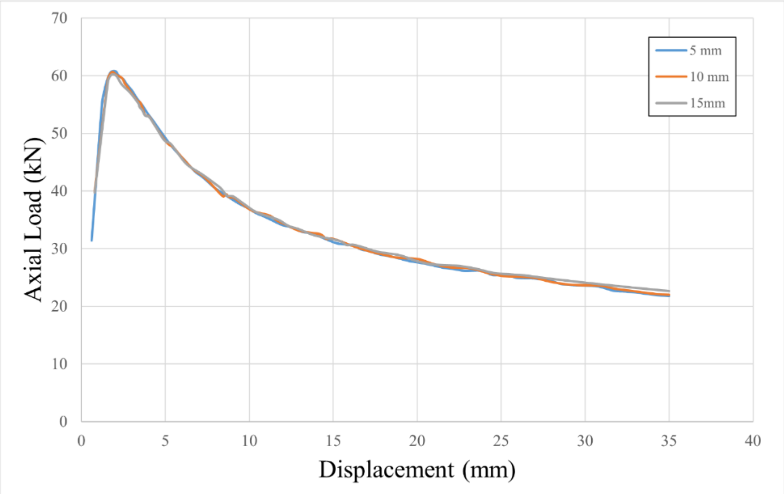

Figure 27. Reaction force variation for different mesh sizes

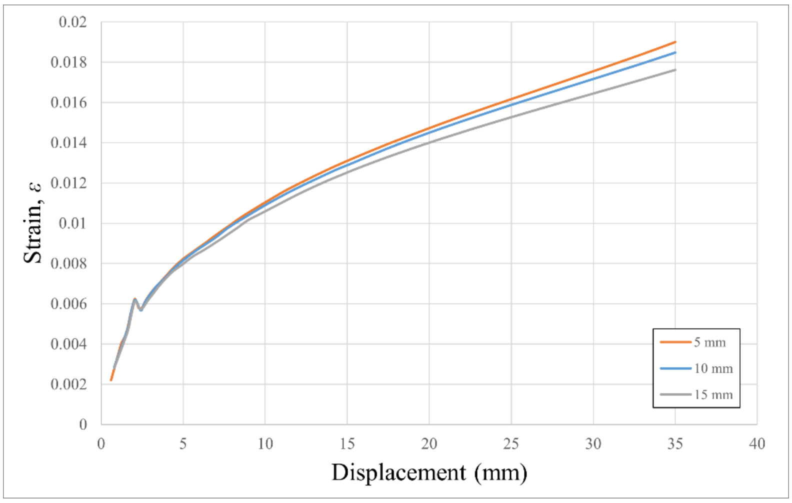

Figure 28. Strain variation for different mesh sizes

3.4. Boundary Conditions and Loading

An idealized fixed boundary condition was employed to enhance computational efficiency and numerical convergence (Figure 29). This was achieved by incorporating multi-point constraint elements (MPC184). The procedure involved identifying master nodes at the center of each pinned end and connecting them to nodes at the edges of the brace model using MPC184. The displacement of the first master node was restricted in the x and z directions, while translation in the y direction and rotation around the z-axis were unrestricted. Similarly, the displacement of the second master node was constrained in all directions except for rotation around the z-axis. Eccentric loads have been applied by moving master nodes in the x direction.

Finally, displacement controlled cyclic loading was applied, and the nonlinear analysis utilized the full Newton-Raphson method. Each load step was divided into multiple sub-steps to incrementally reach the desired displacement level.

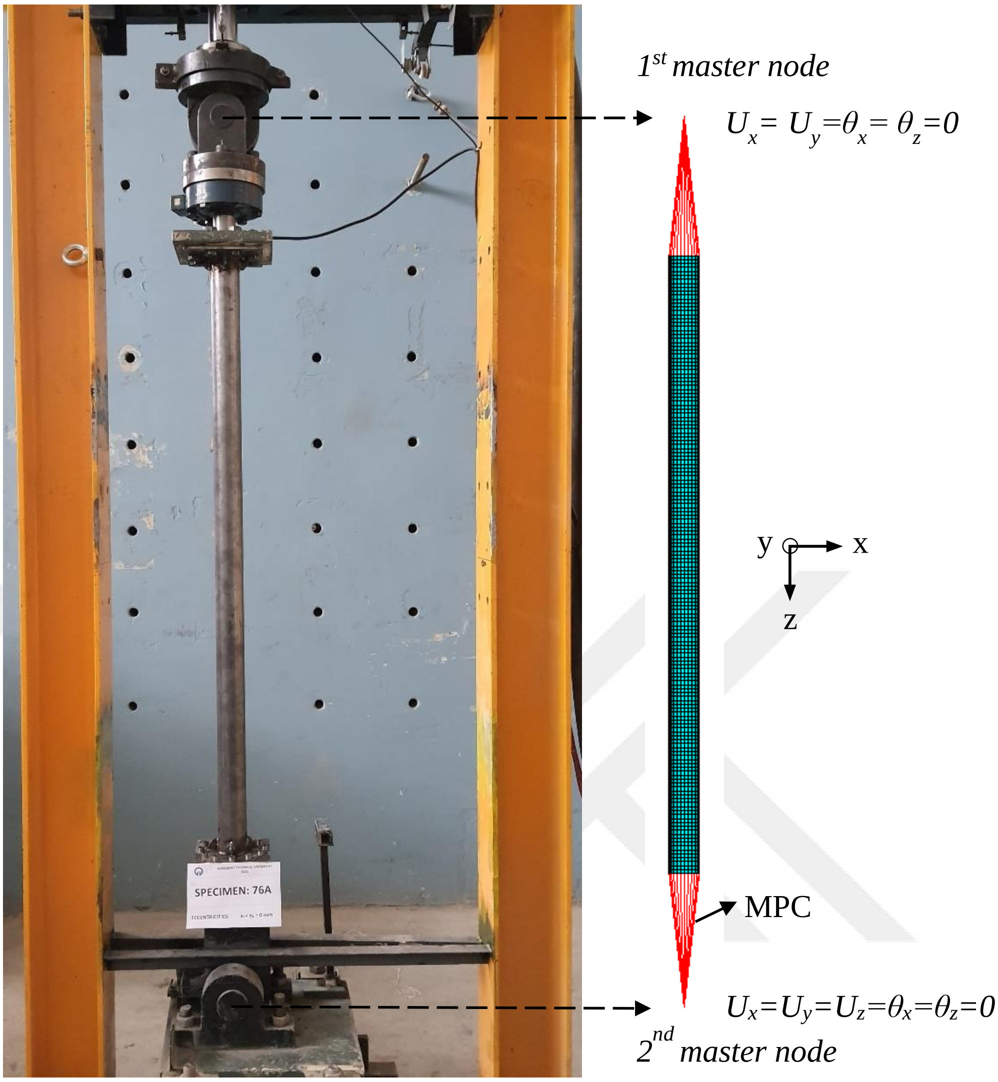

Figure 29. Boundary conditions

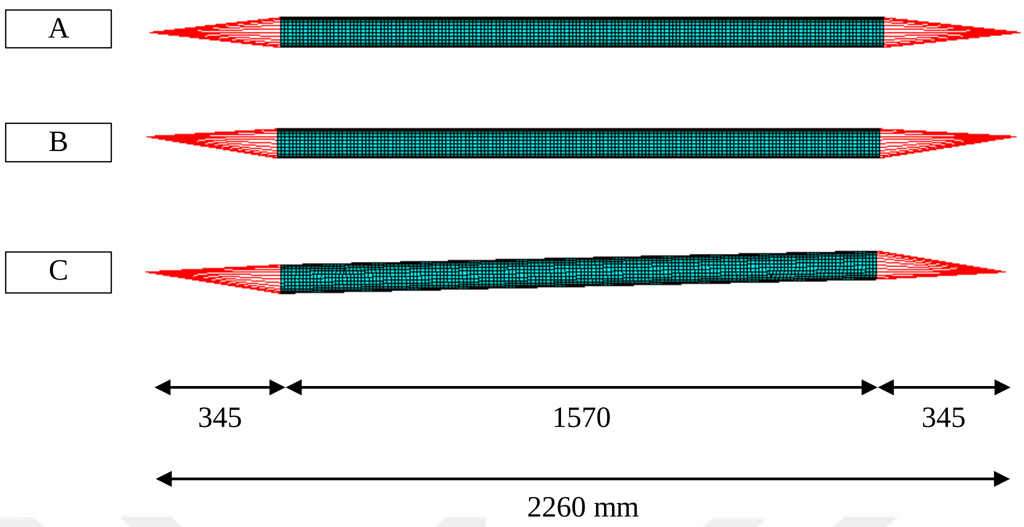

Figure 30. Dimensions and eccentricity conditions of FE models

4. RESULTS AND DISCUSSION

4.1. Experimental Results

In this section, the results obtained from the experimental study carried out to determine the behavior of the specimens under quasi-static cyclic loading are presented. Within the scope of the experimental program, a total of 12 specimens of approximately 1/3 scale were tested. In graphs and tables, "+" indicates compression loading and "-" indicates tensile loading.

4.1.1. 42 Series Specimens

Load-Displacement curves of 42A, 42B, and 42C specimens tested under cyclic loading are presented in Figure 31. The global buckling load (P_b) and the first two post-buckling loads (P_{pb1} and P_{pb2}) are given in Table 6. Specimen 42A exhibited elastic behavior for three cycles and then global buckling occurred at 23.674 kN load level at the 4th cycle. After global buckling, there was a sudden decrease in compressive load. As displacement amplitudes increased, compressive strength gradually decreased relative to the global buckling load. Specimen 42B behaved elastically until the 6th cycle. Subsequently, due to the equal eccentricity condition (Condition-B), 42B exhibited flexural-dominated behavior and reached compressive resistance at the 17.107 kN load level. Even though global buckling did not occur, the straightening effect in tension cycles led to post-buckling in the subsequent cycles, as shown in Figure 33. Referring to Figure 31, the straightening effect has resulted in a significant increase in post-buckling strength. Specimen 42C underwent global buckling at the 4th cycle, which occurred at 23.005 kN load level. As displacement amplitudes increased in the following cycles, post-buckling strength significantly increased compared to the initial buckling load. This phenomenon can also be attributed to the straightening process occurring during tension phases. On the other hand, as seen in Figure 31, while the straightening effect increased the post-buckling load in only 2 cycles for 42B, in the case of 42C, the post-buckling load increased in each cycle.

The yield strength (P_y) for this set of specimens was determined to be 96.52 kN using the equation:

$$P_y = A \cdot f_y \tag{15}$$

where A is the cross-sectional area and f_y is the yield strength. The yield strength values used in this equation were sourced from the tensile test results presented in Table 5.

In the testing process, all 42 specimens reached the yield point in tension by the 8th cycle, while no such occurrence was observed in compression. Additionally, 42 series specimens successfully completed the applied loading protocol without any instances of rupture or local buckling being observed. Figure 34 shows the final phase of the test of series 42 specimens.

Table 6. Experimental results

Specimen		***P_b (kN)***	***P_{pb1} (kN)***	***P_{pb2} (kN)***
42	***A***	23.674	21.500	19.600
	B	17.107	23.813	26.128
	C	23.005	27.973	29.992
48	***A***	34.605	16.572	15.353
	B	18.747	21.636	16.537
	C	24.909	17.320	15.666
60	***A***	54.362	42.247	39.061
	B	34.240	33.300	32.029
	C	43.809	34.215	32.976
76	***A***	98.768	54.867	48.479
	B	47.695	46.181	43.396
	C	66.425	69.611	64.389

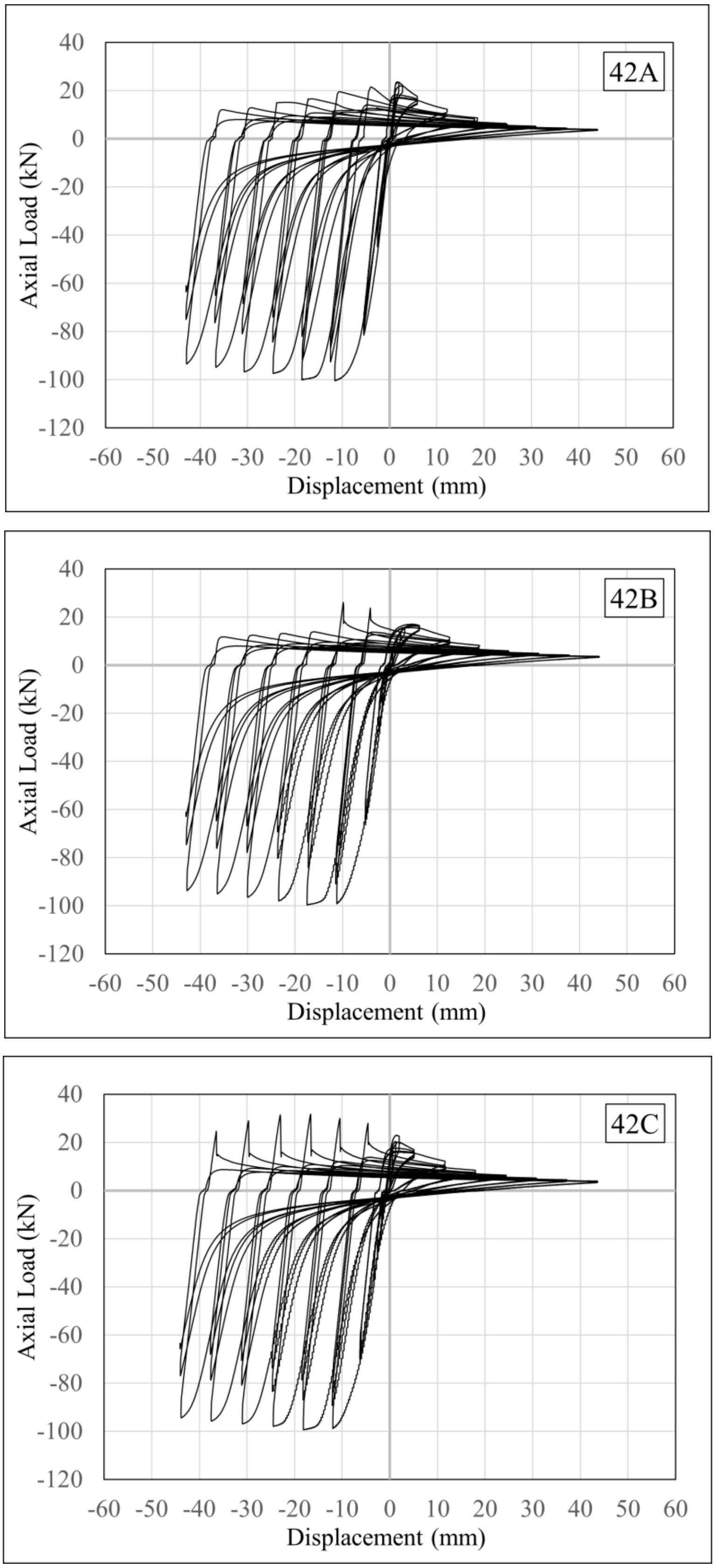

Figure 31. Load-displacement responses of 42 series specimens

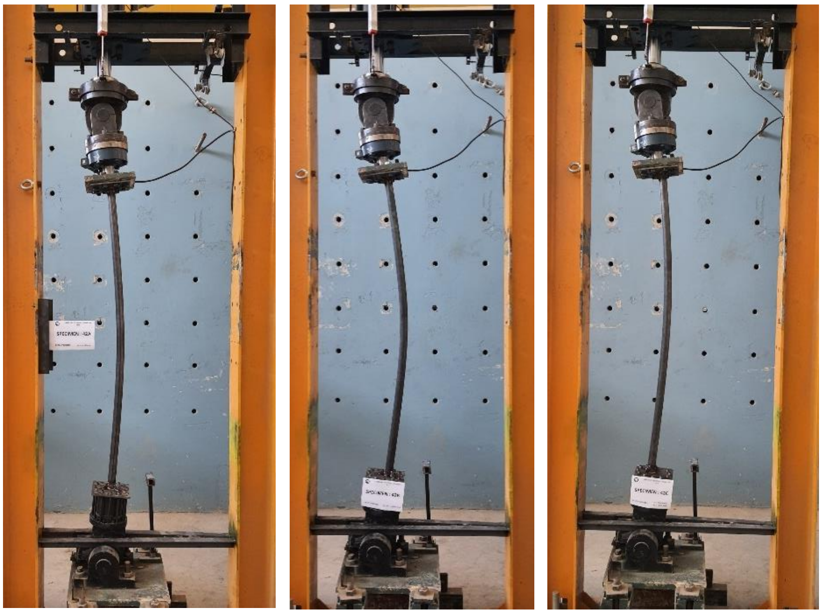

42A @4 | 42B @6 | 42C @4

Figure 32. Global buckling of 42 series specimens

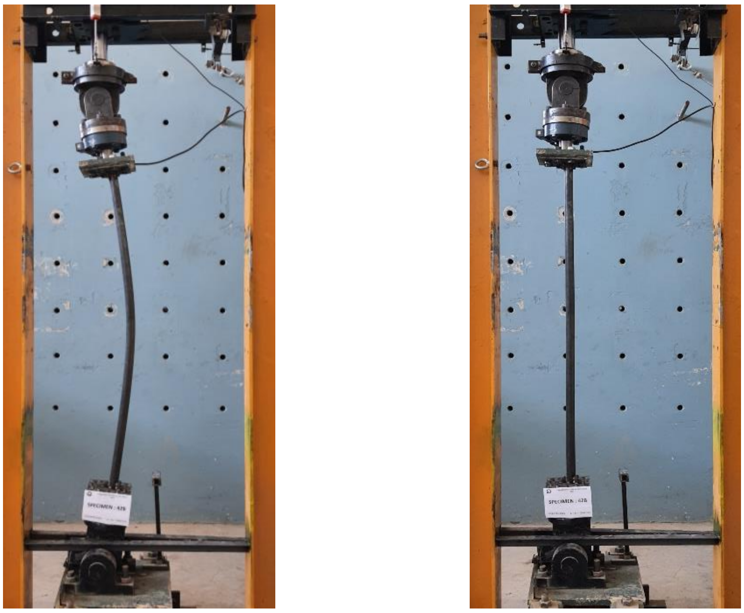

42B Compression phase @11 | 42B tension phase @11

Figure 33. Straightening process

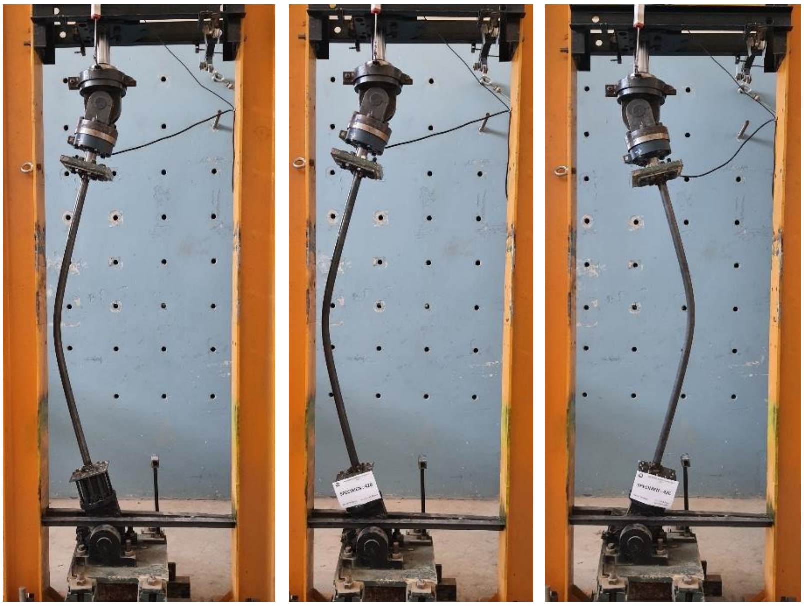

42A @25 42B @25 42C @25

Figure 34. Final phase of 42 series specimens' test

4.1.2. 48 Series Specimens

Load - Displacement curves of 48A, 48B and 48C specimens tested under cyclic loading are given in Figure 35 and the global (P_b) and first two post-buckling loads (P_{pb1} and P_{pb2}) are given in Table 6. 48A experienced global buckling at 34.605 kN during the 3rd cycle. Following this, the buckling strength suddenly decreased to half of its initial value and continued to gradually decrease at the following cycles. Specimen 48B reached its compressive resistance at an applied load of 18.747 kN during the 3rd cycle, primarily due to bending rather than buckling. Subsequent to the cycle a significant increase in load was observed, reaching twice the initial compressive resistance. During this cycle, post-buckling became evident, and this can be attributed to the straightening process that occurred during the tension phase. Following this post-buckling event, the load capacity decreased in comparison to the initial compressive load. 48C experienced global buckling at 24.909 kN load at the 3rd cycle. As displacement amplitudes increased, buckling strength gradually decreased relative to the initial buckling load. Surprisingly, the straightening effect during tensile loading did not lead to an increased post-buckling load as observed in 42C.

The yield strength (P_y) for this set of specimens was determined to be 80.00 kN using Equation 15. 48 series specimens reached the yield point in tension by the 8th cycle, whereas this did not occur in compression. Although local buckling became evident at the 23rd cycle for specimens 48A and 48B, and at the 24th cycle for specimen 48C (Figure 37), the testing process completed without any instances of visible crack around the local buckling zone or rupture. Figure 38 shows the final phase of the test of series 48 specimens.

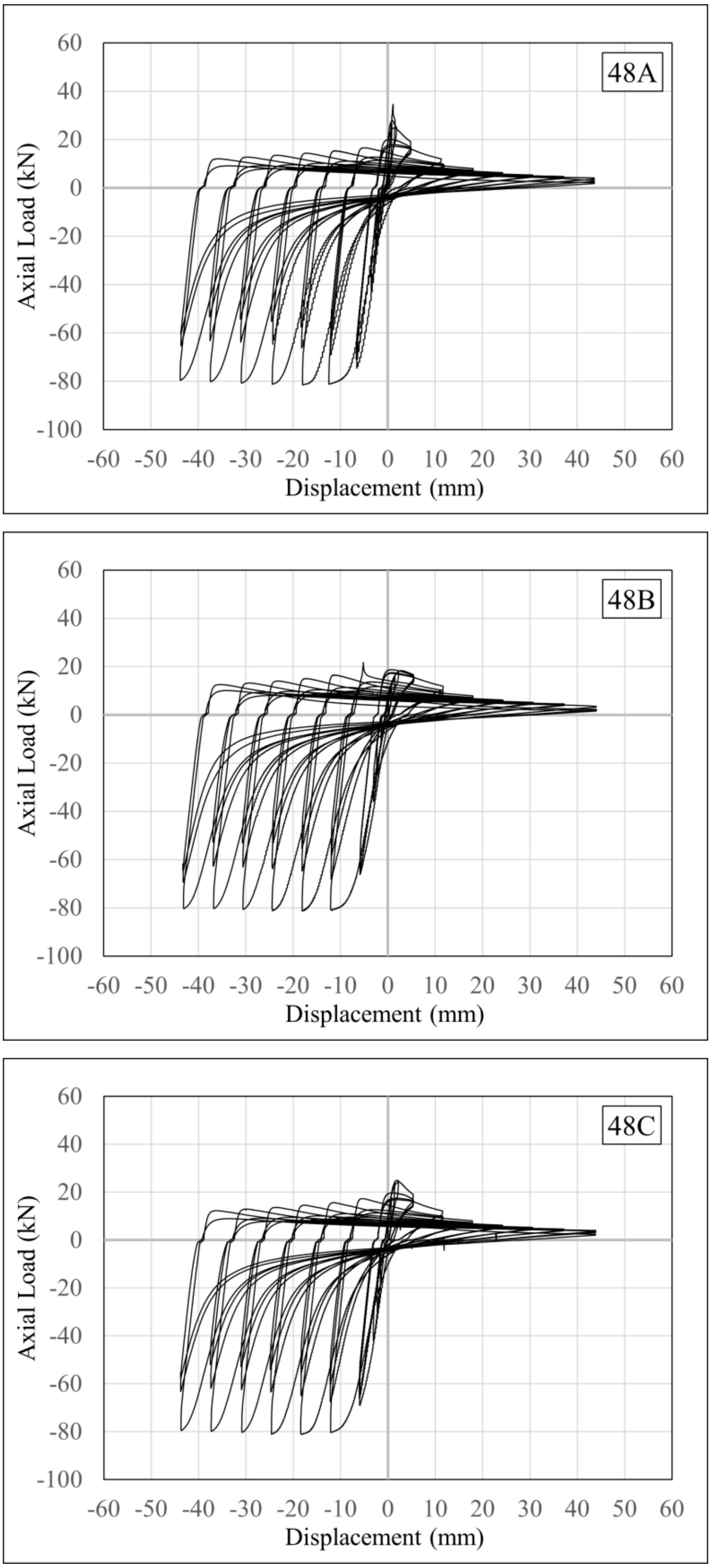

Figure 35. Load-displacement responses of 48 series specimens

48A @3 48B @3 48C @3

Figure 36. Global buckling of 48 series specimens

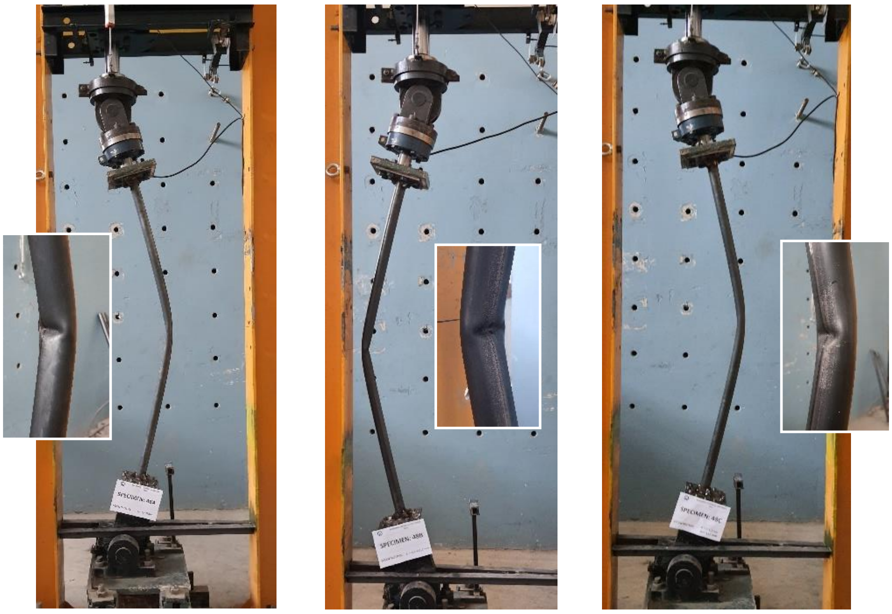

48A @23 48B @23 48C @24

Figure 37. Local buckling of 48 series specimens

48A @25 48B @25 48C @25

Figure 38. Final phase of 48 series specimens' test

4.1.3. 60 Series Specimens

Load - Displacement curves of 60A, 60B and 60C specimens tested under cyclic loading are given in Figure 39. The global (P_b) and first two post-buckling loads (P_{pb1} and P_{pb2}) are given in Table 6. 60A experienced global buckling at the 5th cycle, reaching a global buckling load of 54.362 kN. As displacement amplitudes increased, buckling strength gradually decreased relative to the global buckling load, and local buckling was observed at midspan at the 14th cycle. 60B reached a compressive resistance at 34.240 kN load level due to bending rather than buckling, a consequence of employing eccentricity condition B. Post buckling failure occurred in subsequent compression cycles, mainly due to the straightening effect during tension phases. All recorded buckling strengths at the following cycles remained almost the same with the global buckling load. Local buckling became apparent at midspan during the 15th cycle, and visible cracks were observed around this region. At the 5th cycle, 60C experienced global buckling at a load level of 43.809 kN, resulting in a sudden decrease in load. In the subsequent cycles, the post-buckling load remained relatively constant, primarily due to the straightening effect during tension phases, as the displacement amplitudes increased. Local buckling was recorded at midspan at the 12th cycle.

The yield strength (P_y) for this set of specimens was determined to be 124.66 kN using Equation 15. All the 60 series specimens reached the yield load in tension by the 8^{th} cycle, whereas this did not occur in compression. Additionally, the tests were completed when rupture occurred during the tension phase, specifically in the 17^{th}, 18^{th}, and 16^{th} cycles for specimens 60A, 60B, and 60C, respectively. Figure 42 shows the final phase of the test of series 60 specimens.

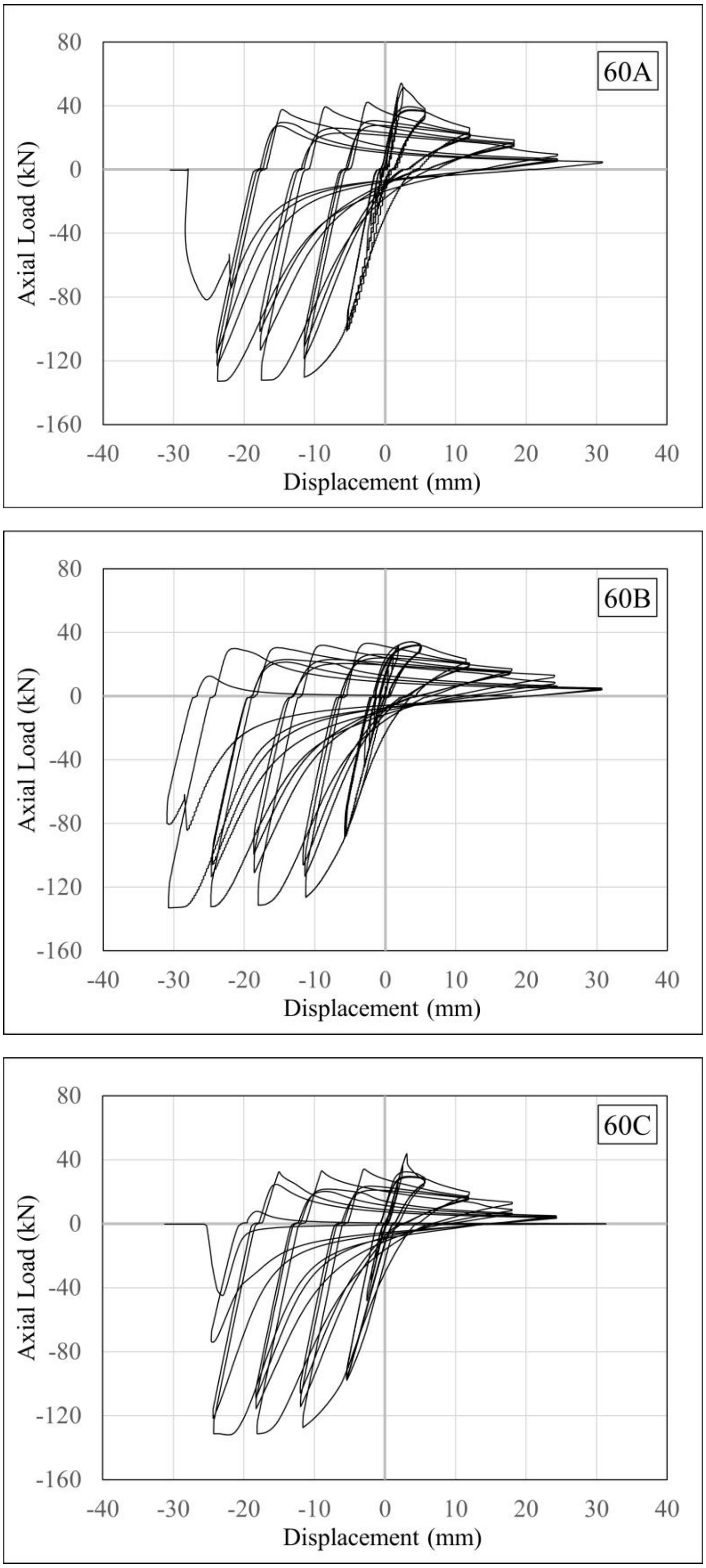

Figure 39. Load-displacement responses of 60 series specimens

60A @5

60B @5

60C @5

Figure 40. Global buckling of 60 series specimens

60A @14

60B @15

60C @12

Figure 41. Local buckling of 60 series specimens

60A @17 60B @18 60C @16

Figure 42. Final phase of 60 series specimens' test

4.1.4. 76 Series Specimens

Load - Displacement curves of 76A, 76B and 76C specimens tested under cyclic loading are given in Figure 43 and the global (P_b) and the first two post-buckling loads are given in Table 6. 76A exhibited elastic behavior for the first 4 cycles and global buckling occurred at the 5th cycle at 98.768 kN load level. Following a significant decrease in buckling strength in the subsequent cycle, post-buckling remained relatively constant as the displacement amplitudes increased. Local buckling was observed at midspan at the 11th cycle. Specimen 76B remained within the elastic region until the 4th cycle, but, unlike 76A, it failed due to bending at 47.695 kN load level at the 5th cycle, a consequence of employing eccentricity condition B. Post-buckling loads remained almost the same with the initial compressive strength as displacement amplitudes increased. Local buckling became evident at midspan at the 11th cycle. Specimen 76C experienced global buckling at load 66.425 kN at the 5th cycle. Subsequent to global buckling, the post-buckling loads remained consistently close to the initial buckling strength. This phenomenon can be attributed to the straightening process occurring during the tension phases. Furthermore, local buckling was observed slightly above the midspan at the 11th cycle.

The yield strength (P_y) for this set of specimens was determined to be 136.03 kN using Equation 15. All the 76 specimens reached the yield load in tension by the 8^{th} cycle, whereas this did not occur in compression. Additionally, the tests concluded when rupture occurred during the tension phase, specifically in the 14^{th}, 15^{th}, and 14^{th} cycles for specimens 76A, 76B, and 76C, respectively. Figure 46 shows the final phase of the test of series 76 specimens.

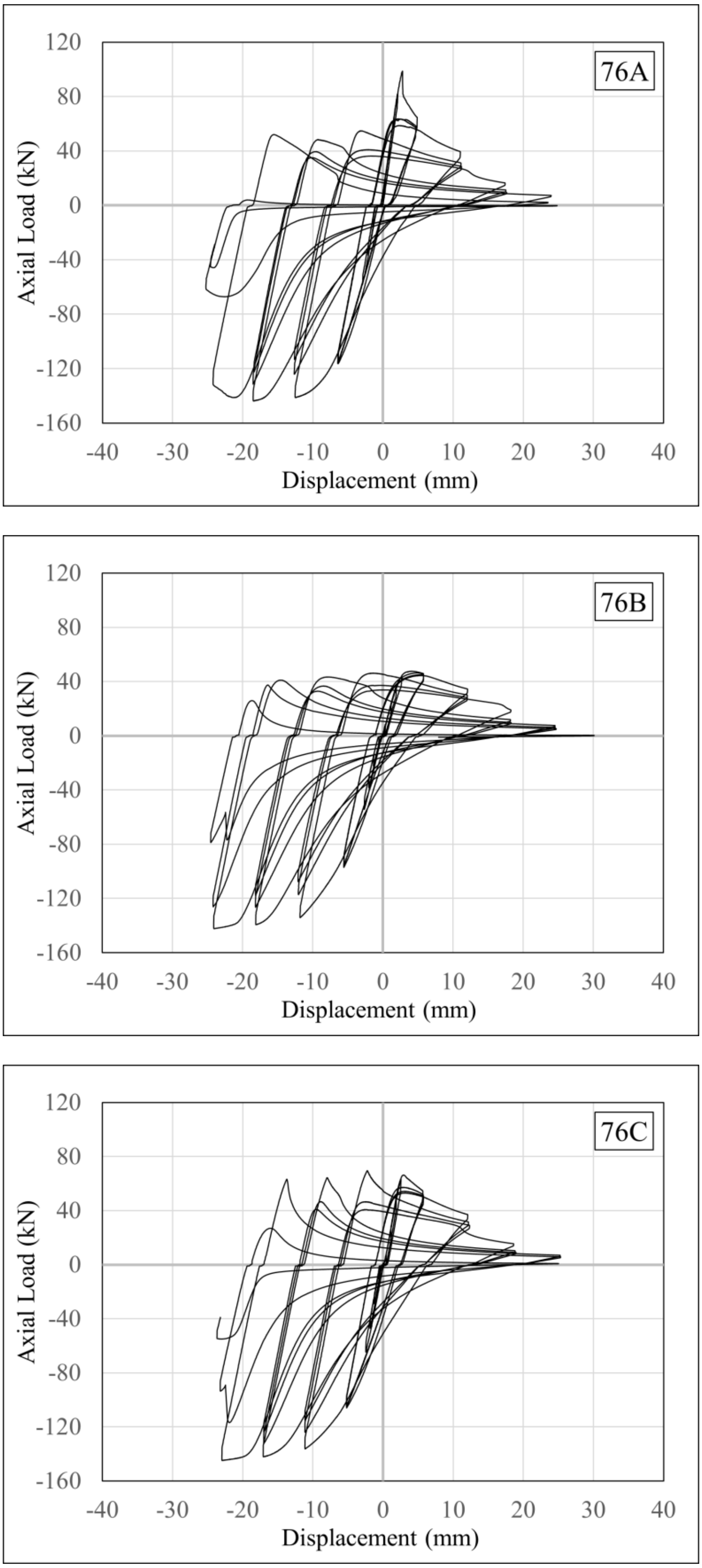

Figure 43. Load-displacement responses of 76 series specimens



76A @5 | 76B @4 | 76C @5

Figure 44. Global buckling of 76 series specimens



76A @11 | 76B @11 | 76C @11

Figure 45. Local buckling of 76 series specimens

76A @14 76B @15 76C @14

Figure 46. Final phase of 76 series specimens' test

4.2. Evaluation of Experimental Results

4.2.1. Buckling Load

The variation in buckling strengths due to eccentricity conditions is presented in Figure 47. It is observed that in all the tested specimens, the highest buckling strength was recorded in condition A (concentric load), as expected. Conversely, the lowest buckling strength was observed in eccentricity condition B, while a relatively higher buckling strength was recorded in condition C. This matches the findings of Albero et al. (2022)'s findings regarding unequal eccentricity. Figure 47 shows that the declining trend in buckling strength caused by eccentricity is consistent across all specimens. Furthermore, it is evident that the impact of eccentricity on buckling strength diminishes as the slenderness ratio increases.

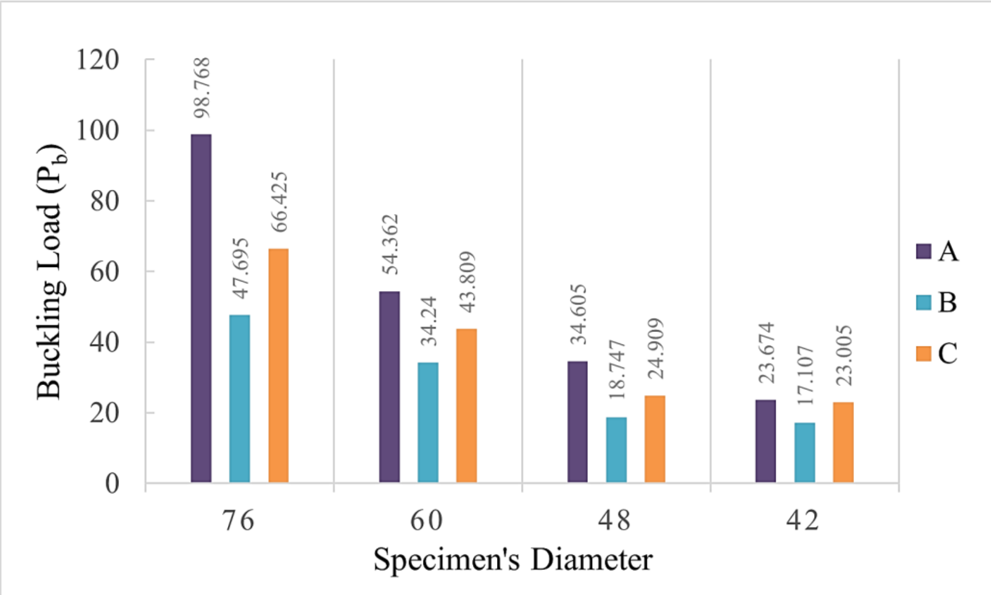

Figure 47. Buckling load (P_b) variation of test specimens

To facilitate comparisons of buckling loads with design codes on a single chart, the values of buckling loads and slenderness ratios were normalized. The comparison of buckling loads with the unfactored design loads provided by AISC 360-22 (2022) and EN 1993-1-1 (2005) is presented in Figure 48. It is important to highlight that B specimens with a normalized slenderness ratio of up to 1.5 do not meet the requirements specified by both codes. Meanwhile, for the specimen series with a slenderness of 1.68 (denoted as series 42), it falls between the AISC and EC3 curves, satisfying only the EC3. Moving on to condition C, sets 48, 60, and 76 of specimens comply with the EC3 but are deemed unsafe according to the AISC code. Only the 42 series of specimens meet the criteria outlined by both codes under condition C.

Notably, the influence of eccentricity undergoes a shift at normalized slenderness levels of 1.5. Beyond this threshold, the impact on buckling strength concerning design codes decreases.

In general, Figure 48 indicates that significant reductions in buckling strength occur even at low eccentricity values, highlighting the need for more conservative codes in addressing these scenarios.

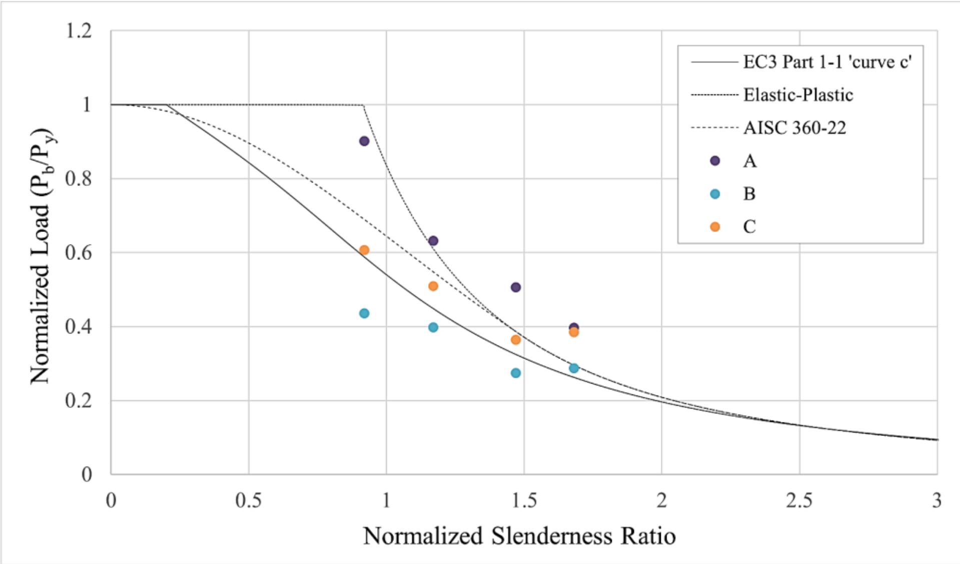

Figure 48. Normalized buckling loads vs. design codes

4.2.2. Post-buckling Strength

The investigation of the post-buckling strength of CHS members is crucial for various reasons, including evaluating the forces developed in other frame members such as beams and columns (Zhou et al., 2018). The inelastic stage of a structure, characterized by nonlinear behavior, becomes especially relevant during seismic events or dynamic loads, emphasizing the importance of understanding how these members behave. Knowledge of post-buckling behavior is instrumental in predicting how bracing elements deform, dissipate energy and transfer loads, ultimately influencing the overall lateral stability of the building.

The first two post-buckling strengths were extracted from the load-displacement graphs for all specimens, normalized, and subsequently compared to AISC 360-22. In accordance with AISC 360-22, approximately 30% of the initial buckling strength signifies the average nominal post-buckling resistance in axially loaded members subjected to cyclic loading, regardless of brace geometric configuration and ductility level.

Figure 49 illustrates the variation in first post-buckling resistances (P_{pb1}) under different eccentricity conditions. It is evident that eccentricity predominantly influences non-slender specimens, with the impact diminishing until 1.5 slenderness levels. Conversely, eccentricity has a positive effect on slender members with a normalized slenderness ratio greater than 1.5.

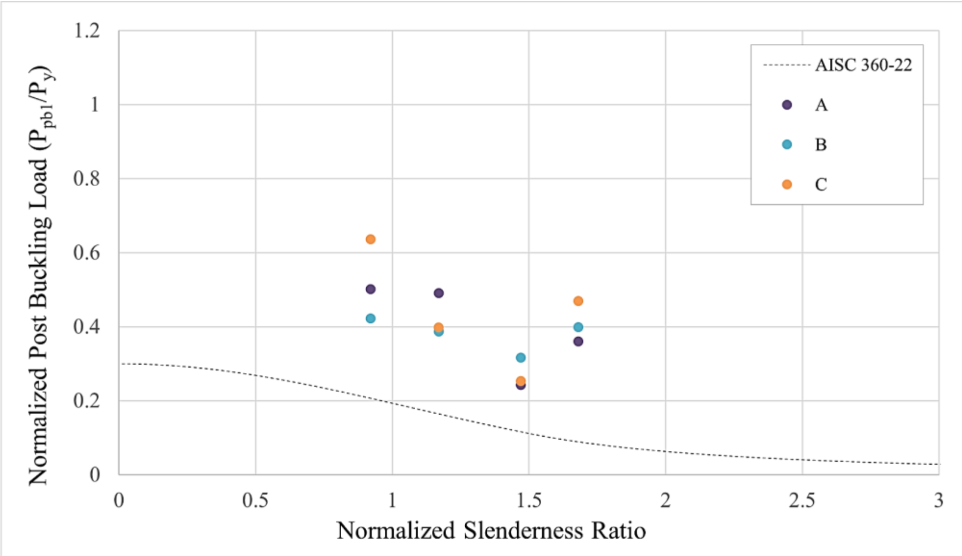

Figure 49. First post-buckling (P_{pb1}) vs. AISC 360-22

In Figure 50, the second post-buckling strengths (P_{pb2}) are compared with AISC 360-22, considering the three eccentricity conditions. Similar to the first post-buckling strengths, the impact is negative when the normalized slenderness ratio is less than 1.5 and positive when it exceeds 1.5.

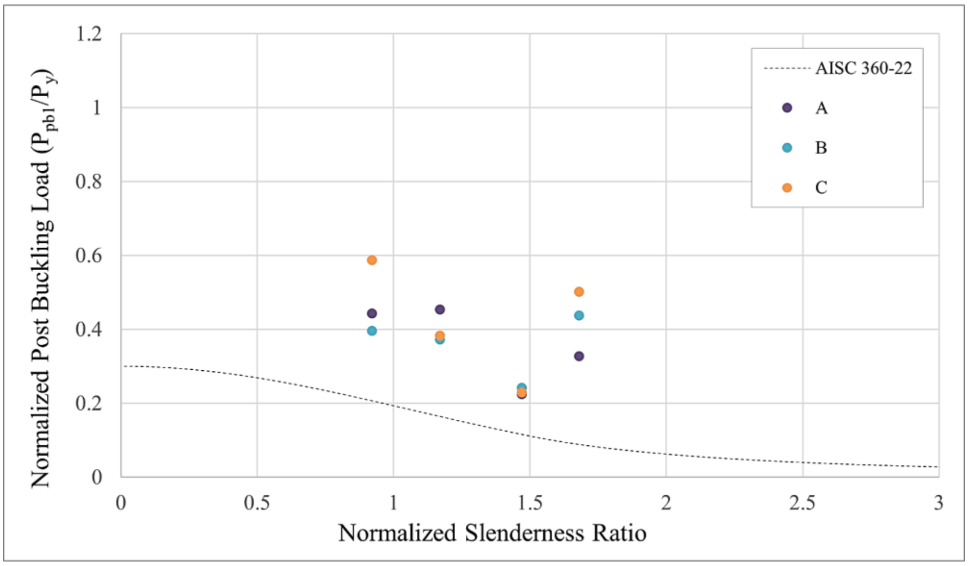

Figure 50. Second post-buckling (P_{pb2}) vs. AISC 360-22

4.2.3. Energy Dissipation Capacity

Energy dissipation, especially in dynamic situations like earthquakes, is a vital indicator for evaluating specimen performance. The energy dissipation capacity of CHS specimens was measured by calculating the area under the hysteresis loops for each cycle and then summing these values to find the total energy dissipation (E). To compare the effect of different eccentricity conditions on the energy dissipation capacity of the braces, the total energy was normalized by dividing it by the elastic energy ($E_y = 0.5P_y\Delta_y$), where Δ_y represents the yield displacement obtained by multiplying the yield strain, ε_y, by the clear length of the specimen, L_b.

Figure 51 presents the comparison of the normalized energy for each specimen. It's worth noting that there is no significant variation observed among specimens of the same diameter. Therefore, it can be concluded that low eccentricity had no impact on energy dissipation.

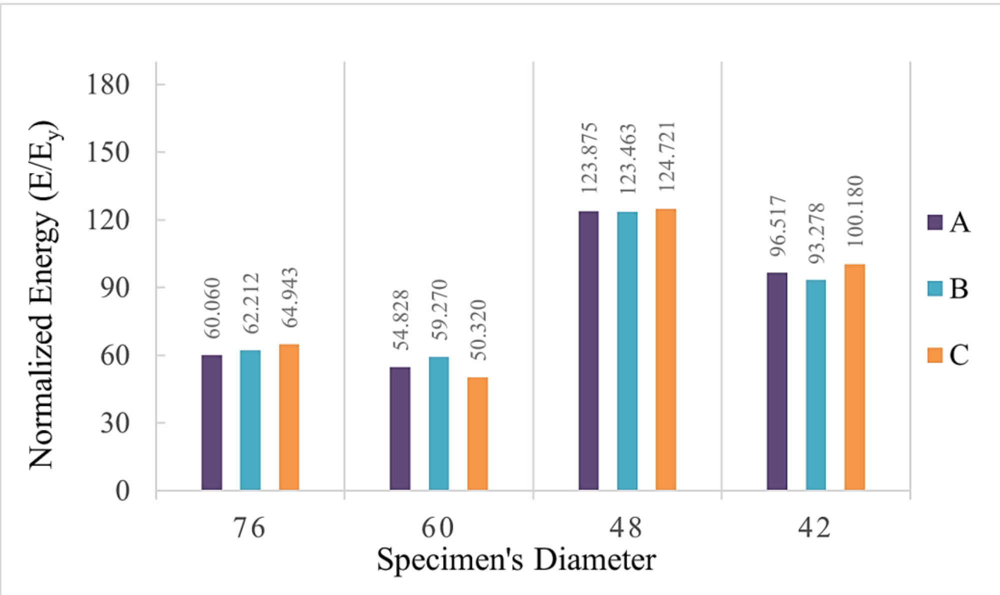

Figure 51. Normalized energy dissipation capacities of test specimens

4.2.4. Initial Stiffness

The consideration of stiffness in structural members is considered important during the design phase as it plays a critical role in ensuring the stability, durability, and safety of structures. In this study, the initial stiffness of test specimens was determined by calculating the slope of their elastic cycles. A significant reduction in stiffness was observed in the specimens when subjected to load eccentricity, as depicted in Figure 52. Across all diameters, a consistent pattern of stiffness variation was evident, with stiffness peaking in condition A, undergoing a considerable reduction in condition C, and reaching its minimum in condition B. These findings offer crucial insights for design, emphasizing the importance of considering these accidental eccentricity scenarios during the design phase to ensure structural stability.

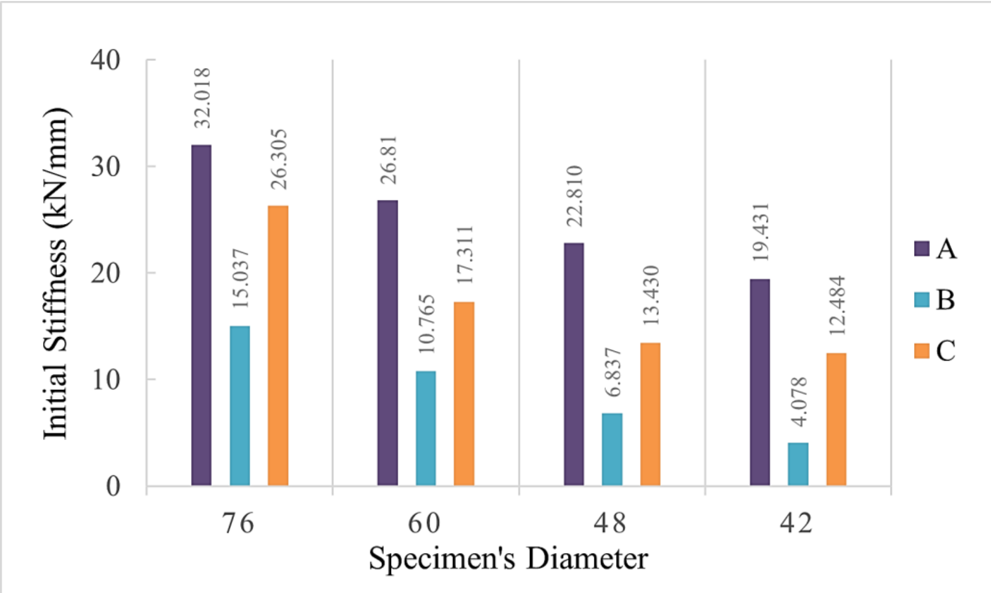

Figure 52. Initial stiffness of test specimens

4.3. Validation of Numerical Results

In this section, the validation procedure for the finite element models outlined in Chapter 3 is conducted to assess their capability in predicting the behavior of CHS specimens. A comprehensive analysis of 12 finite element models corresponding to experimental specimens was conducted. Load-displacement curves were obtained and subsequently compared with the experimental results by placing both the experimental and numerical curves on a unified graph. Comparative evaluations are presented for specimen sets 42, 48, 60, and 76 in Figures 53 through 56. Corresponding error values of global buckling (P_b) are provided in Table 7. The error values, calculated with respect to the experimental results, demonstrate that the developed FE models provide a satisfactory level of accuracy in predicting buckling load, with an error margin consistently around 5%. An exception to this trend is observed in specimen 76B, which exhibits a slightly larger percentage of error. Furthermore, Figures 57 to 60 compare the buckling behaviors and corresponding deformed configurations resulting from the experiments and analyses. These figures also present the first principal total mechanical strain results for the buckling region of the models.

In summary the comparison of experimental and numerical curves indicates that the finite element simulations show adequate agreement with laboratory tests in terms of overall cyclic behavior, buckling load and tensile strength.

Table 7. Error percentages

Specimen		**Numerical P_b (kN)**	**Experimental P_b (kN)**	**Error (%)**
42	**A**	23.227	23.674	1.89
	B	17.526	17.107	2.45
	C	24.274	23.005	5.52
48	**A**	33.096	34.605	4.36
	B	19.664	18.747	4.89
	C	24.46	24.909	1.80
60	**A**	52.432	54.362	3.55
	B	35.221	34.240	2.87
	C	43.689	43.809	0.27
76	**A**	99.988	98.768	1.24
	B	44.803	47.695	6.06
	C	66.768	66.425	0.52

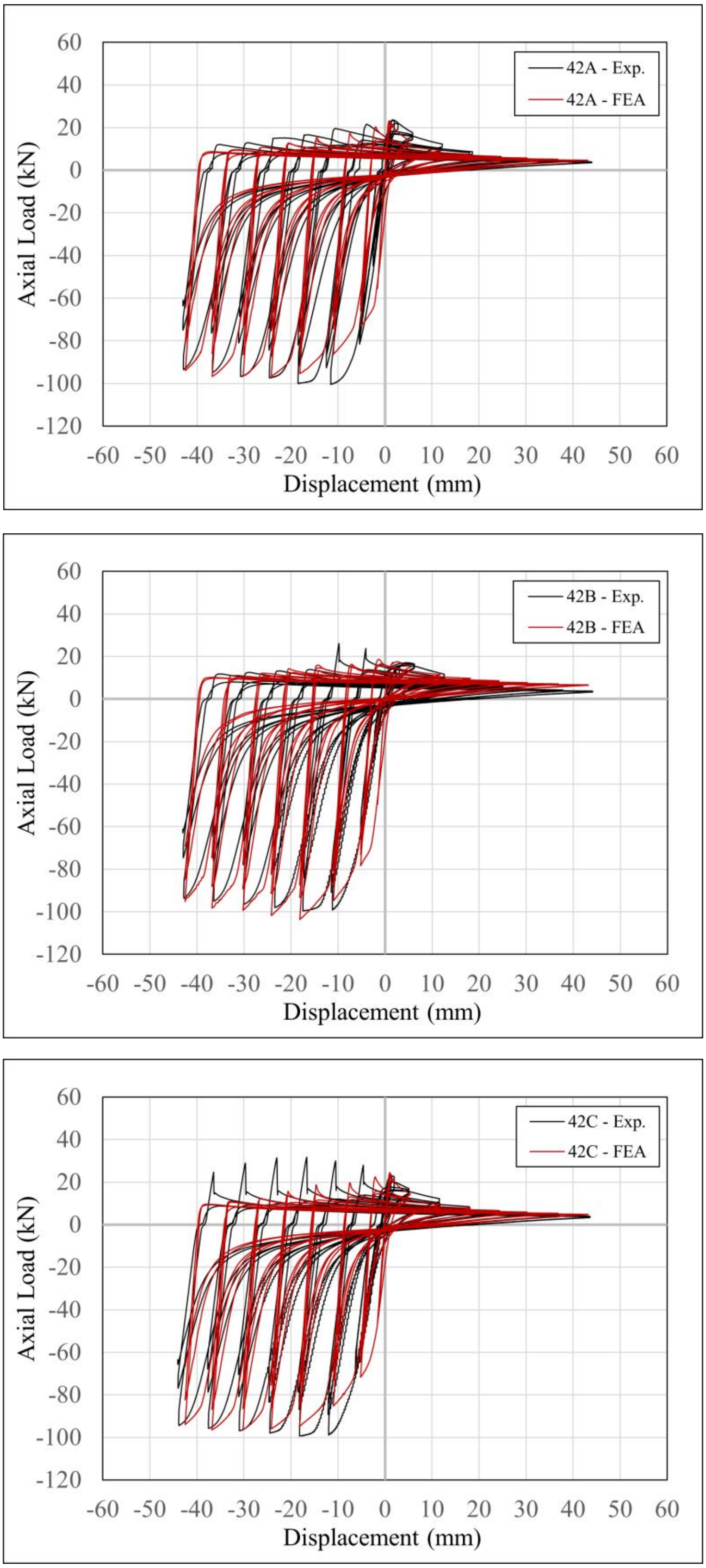

Figure 53. Numerical vs. experimental curves: 42 series specimens

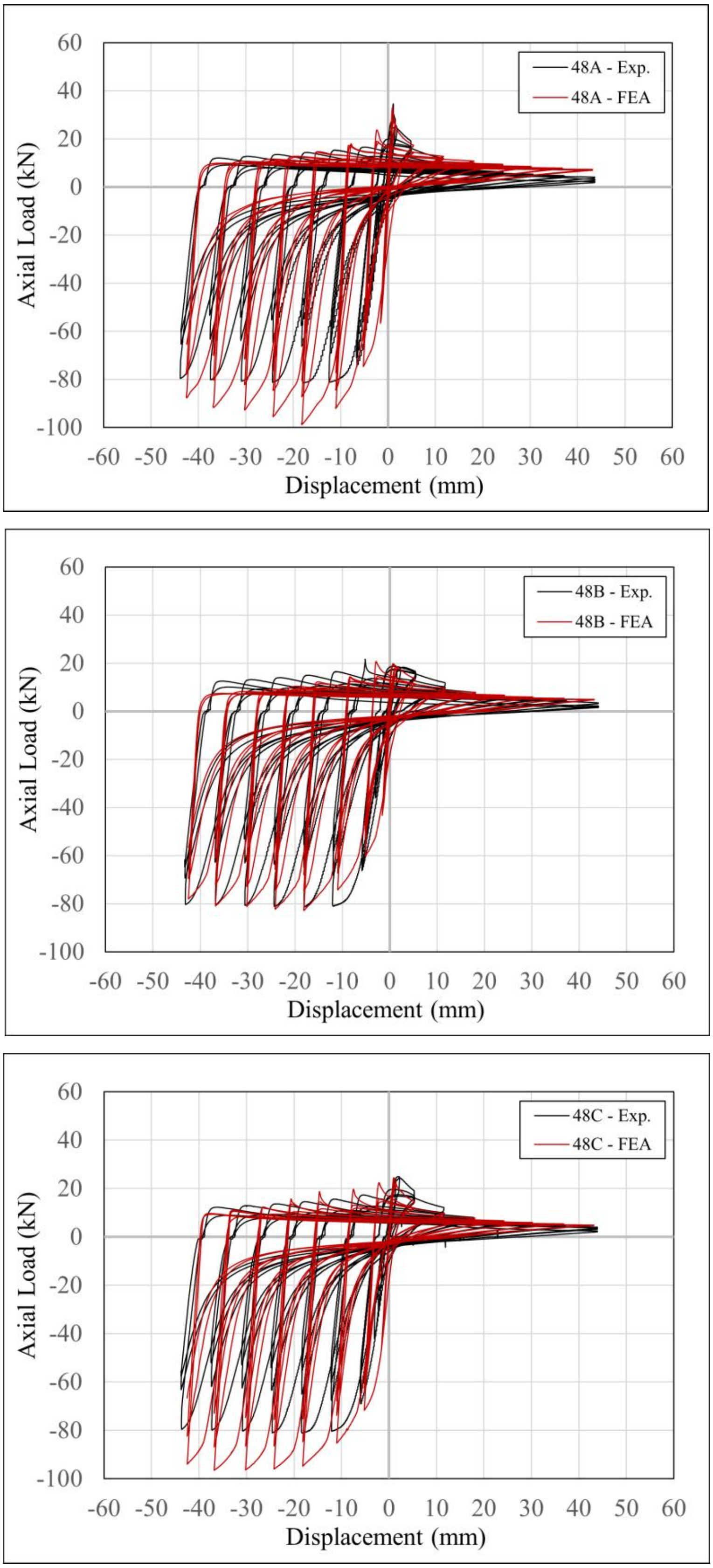

Figure 54. Numerical vs. experimental curves: 48 series specimens

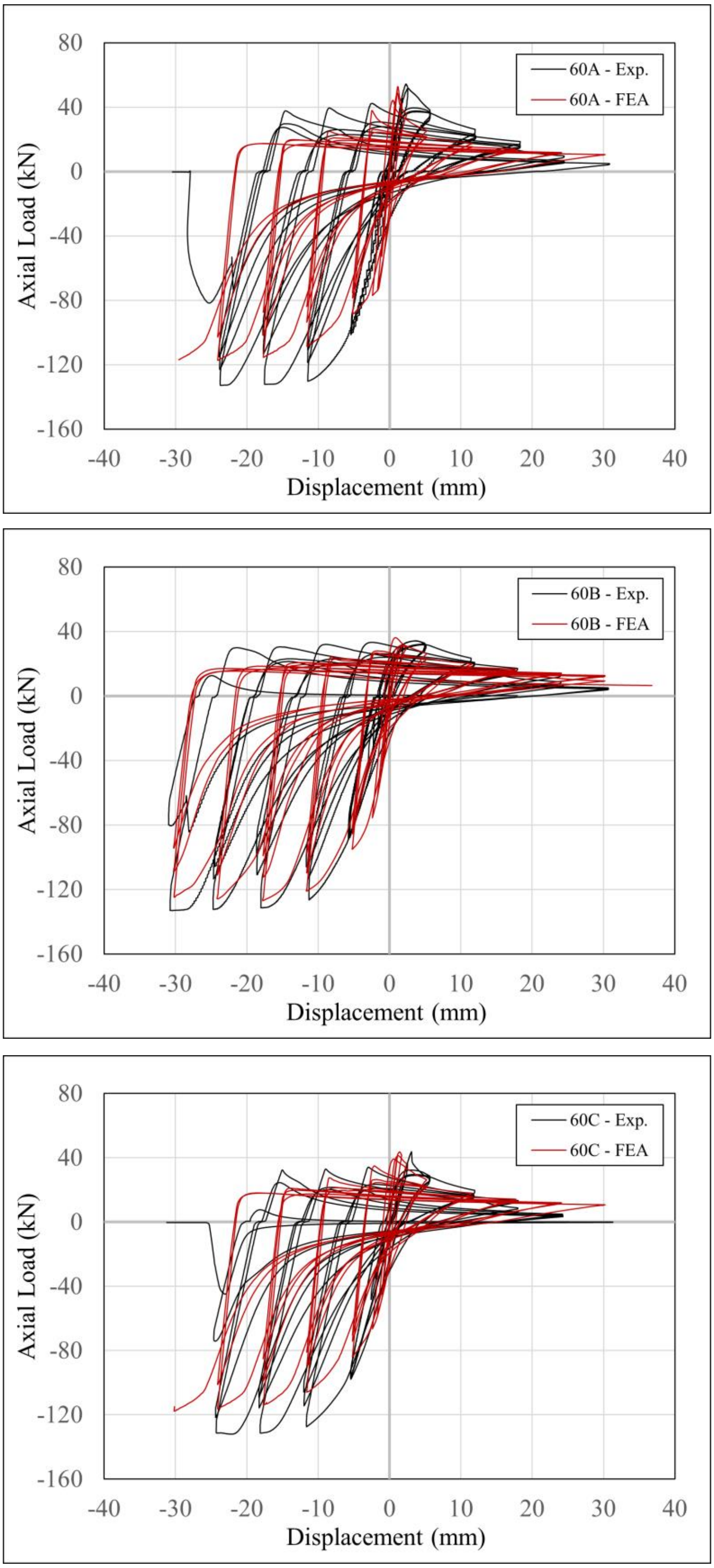

Figure 55. Numerical vs. experimental curves: 60 series specimens

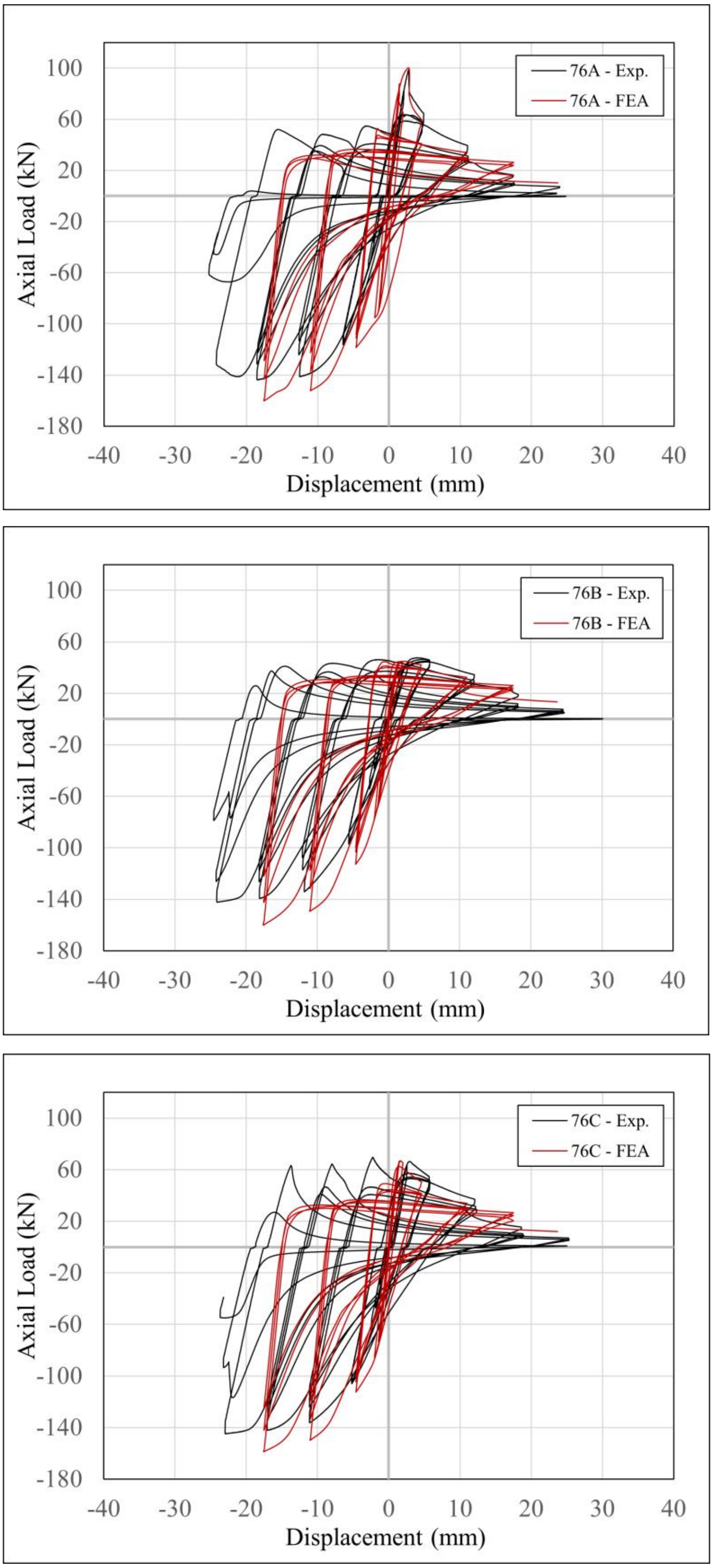

Figure 56. Numerical vs. experimental curves: 76 series specimens

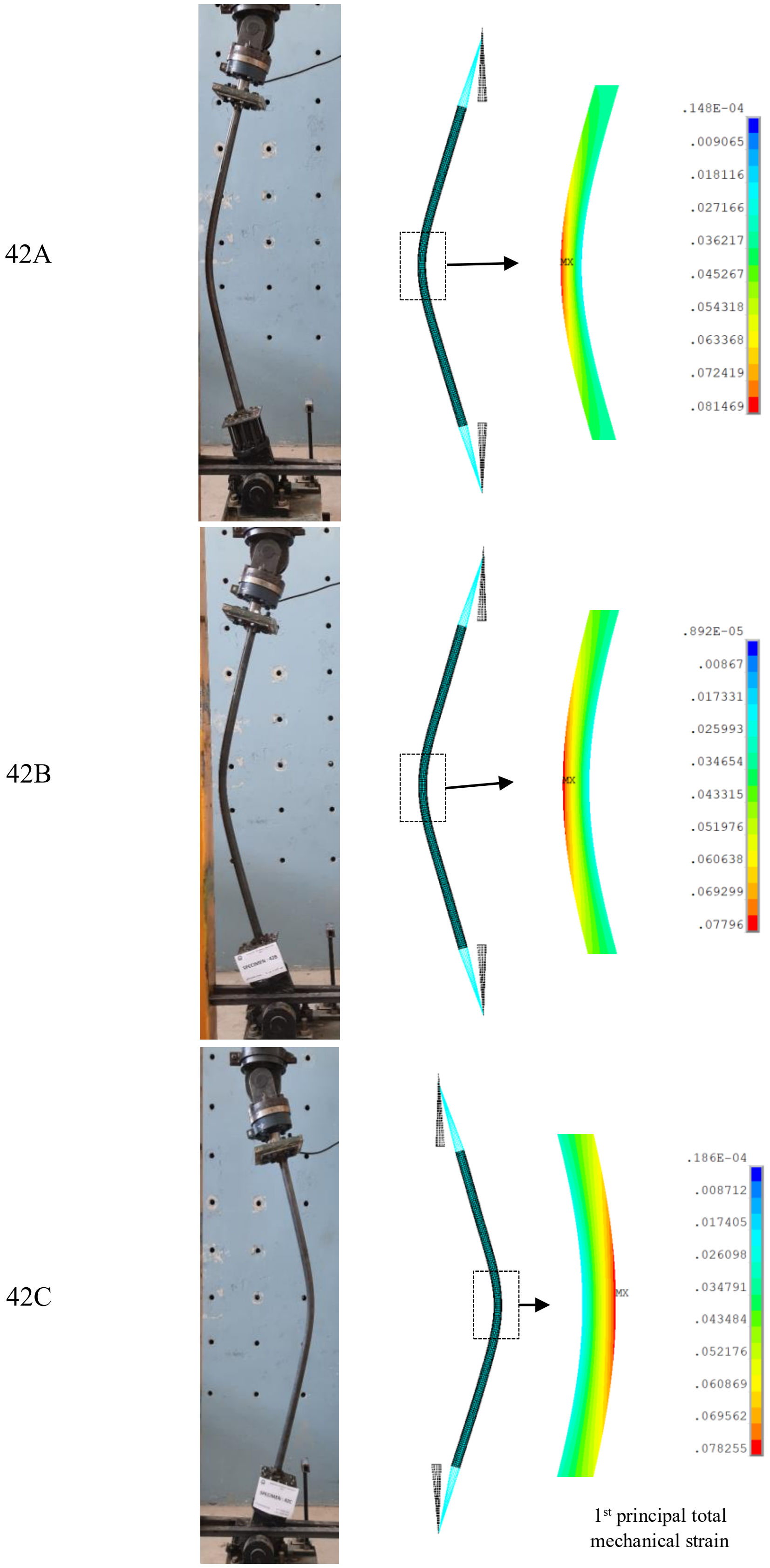

Figure 57. Numerical vs. experimental behavior: 42 series specimens

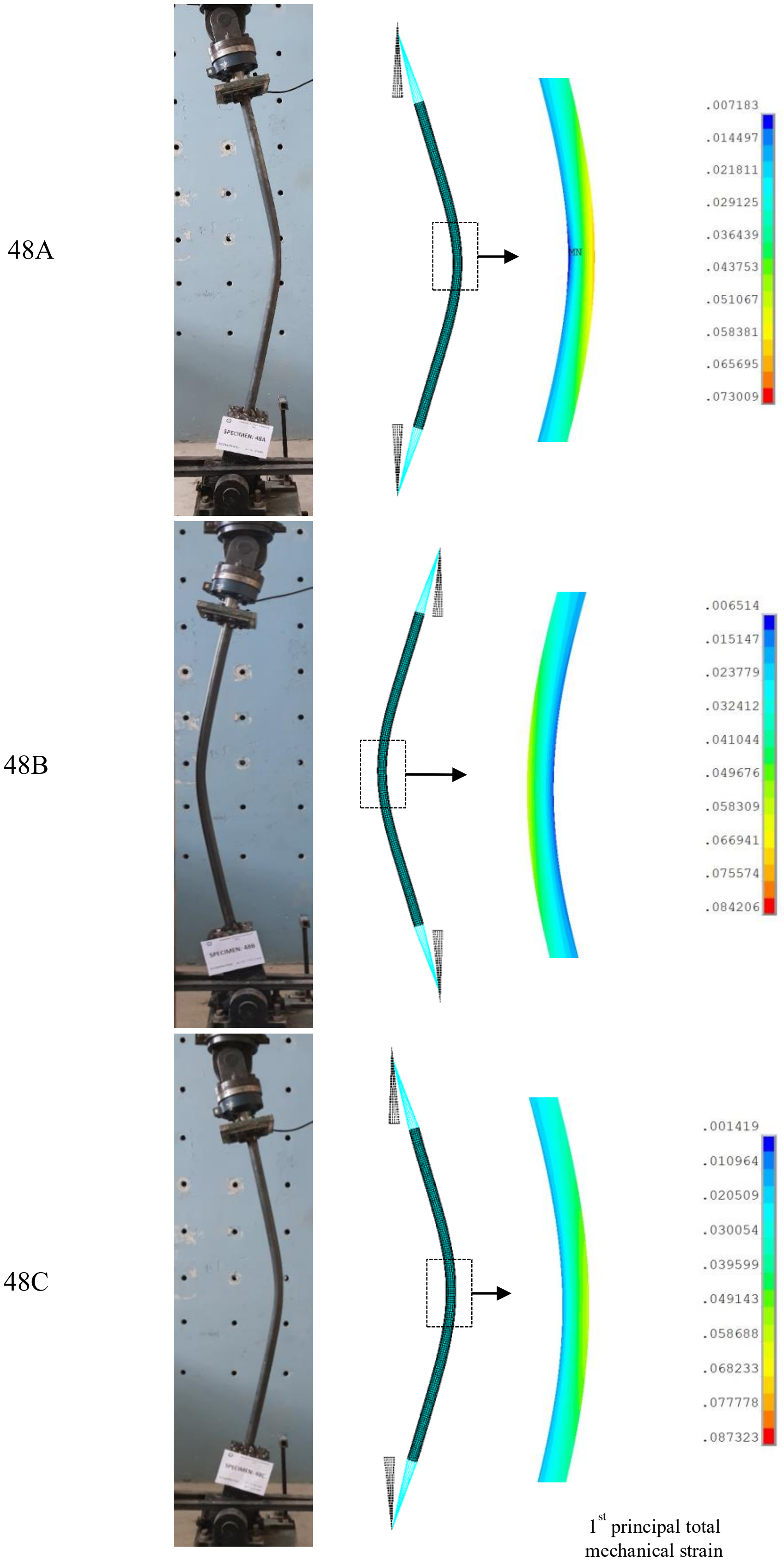

Figure 58. Numerical vs. experimental behavior: 48 series specimens

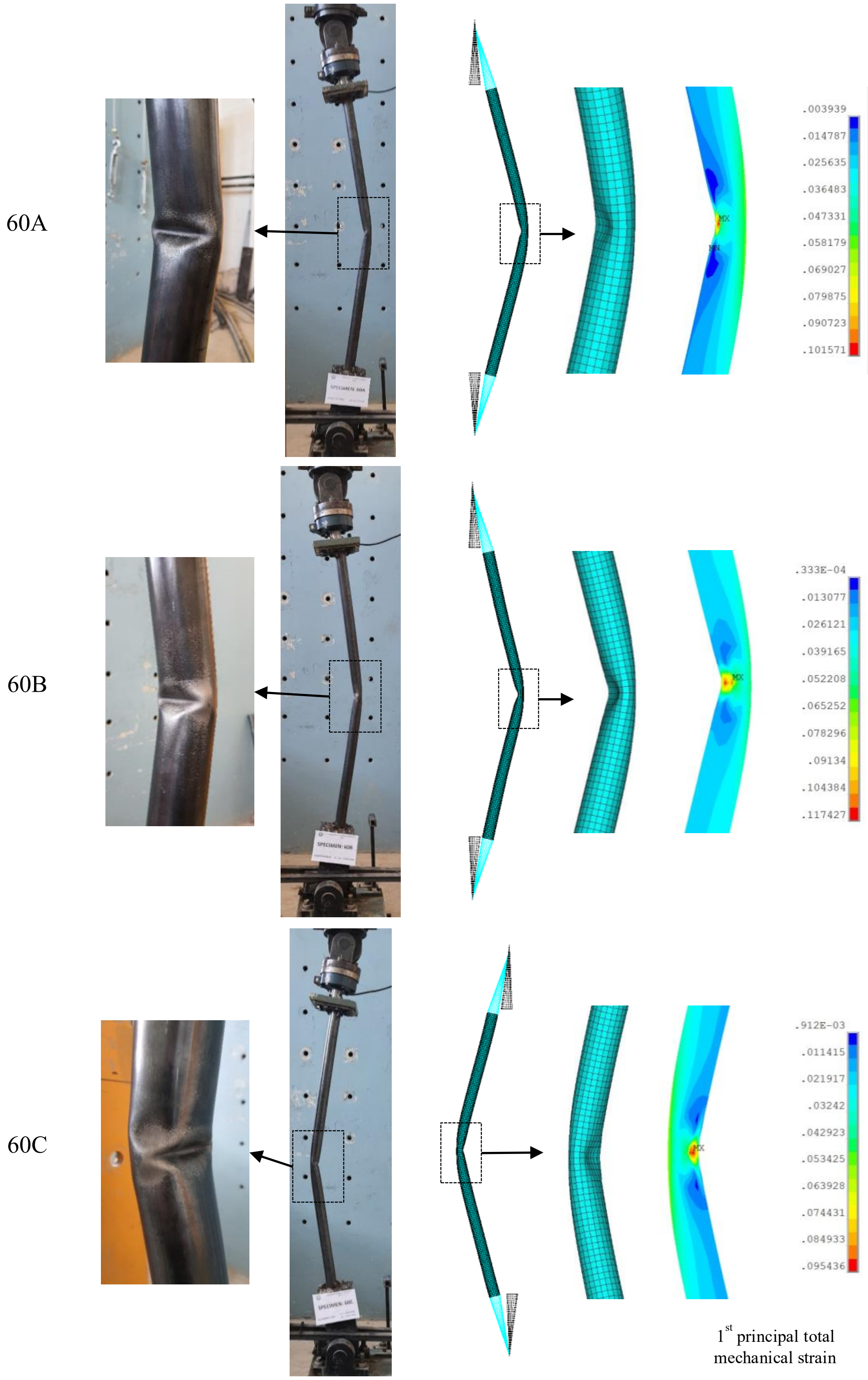

Figure 59. Numerical vs. experimental behavior: 60 series specimens

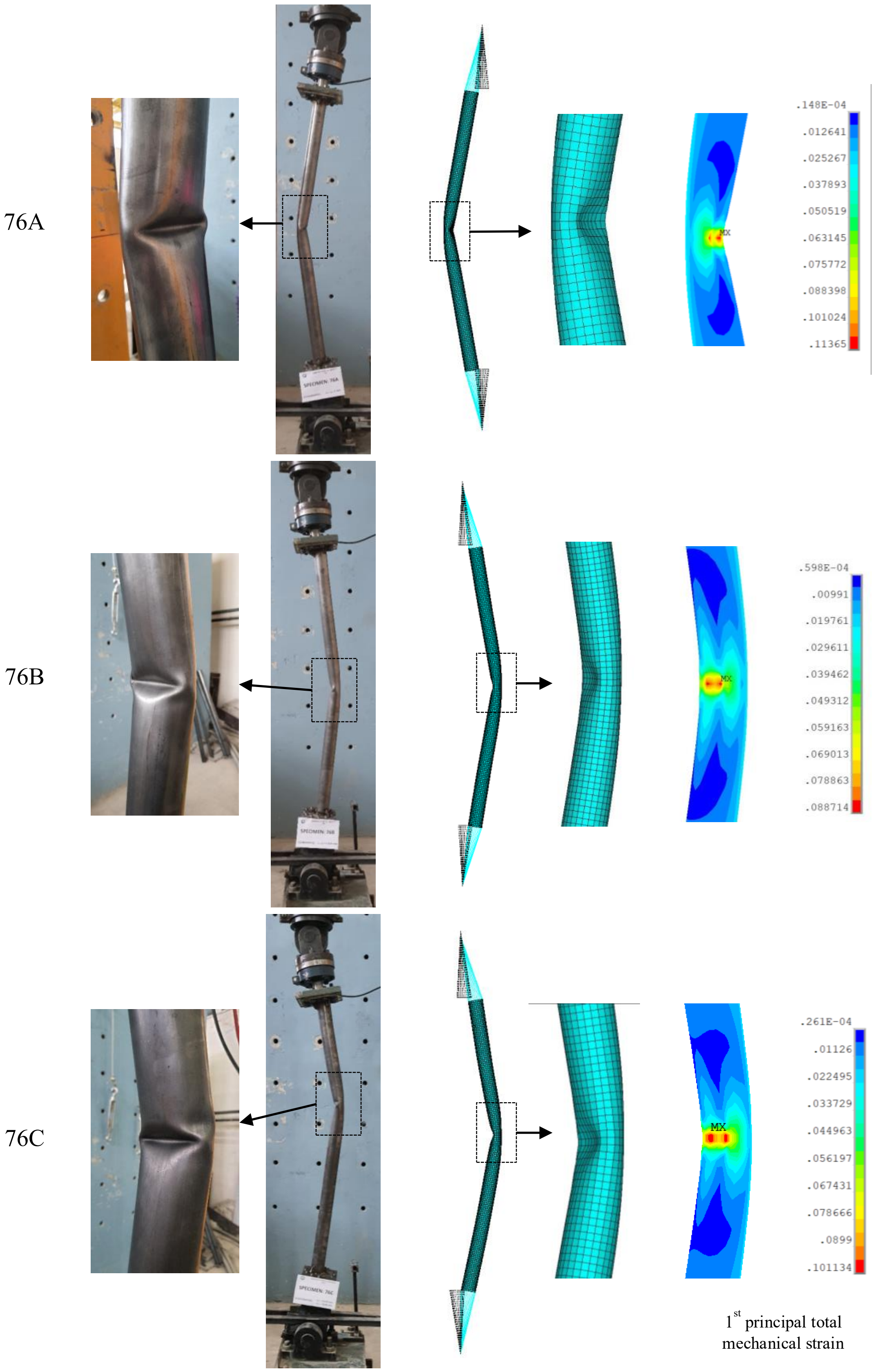

Figure 60. Numerical vs. experimental behavior: 76 series specimens

4.4. Parametric Study

Following the validation study, a comprehensive parametric study was undertaken to assess the influence of various eccentricity values across an expanded slenderness ratio on the axial cyclic response of CHS models. The thickness and length of the members, along with the modelling strategies, including considerations for boundary conditions and loading protocol, are identical to those used in the numerical studies given in Chapter 3.

In the parameter matrix, two additional CHS diameters (88.9x2 and 33.7x2) were introduced existing models, resulting in a global slenderness ratio ranging from 0.79 to 2.15. For conditions B and C across all specimens, two additional eccentricities, namely *0.5e* and *1.5e*, were considered, as detailed in Table 8. This approach ensured a systematic exploration of the effects of eccentricity values within the specified slenderness range on the behavior of CHS members.

Table 8. Parameter matrix

Parameters	**Details**
Length (mm)	1570
Cross-section (mmxmm)	88.9x2, 76.1x2, 60.3x2, 48.3x2, 42.4x2, 33.7x2
Eccentricity	0.5e, 1e, 1.5e
Total number of models	42

4.4.1. Results

In this section normalized buckling loads obtained from the parametric study were assessed. The results of the 42 finite element models derived from the parametric study are given in Table 9.

Table 9. Results of the parametric study

Specimen		P_b (kN)		
		0.5e	***1e***	***1.5e***
33	**A**	11.997	11.997	11.997
	B	10.515	9.463	8.321
	C	13.201	12.113	10.710
42	**A**	23.227	23.227	23.227
	B	19.562	17.526	14.997
	C	24.849	24.274	23.226
48	**A**	33.096	33.096	33.096
	B	26.206	19.664	16.131
	C	32.274	24.460	23.740
60	**A**	52.432	52.432	52.432
	B	40.645	35.221	27.633
	C	49.430	43.689	38.393
76	**A**	99.988	99.988	99.988
	B	56.358	44.803	37.416
	C	75.041	66.768	61.850
88	**A**	131.518	131.518	131.518
	B	70.010	57.019	50.644
	C	93.141	85.267	78.644

Firstly, an investigation was conducted to assess the variation in buckling strengths of *1e* eccentricity conditions across the extended range of slenderness ratios, as illustrated in Figure 61. The results reveal a consistent pattern in alignment with experimental findings. Specifically, the buckling strengths of the newly introduced CHS models maintained a trend wherein eccentricity exhibited the most notable influence on non-slender models, with this impact diminishing as slenderness increased. According to these results, Condition B is considered unsafe for both codes up to a slenderness ratio of 1.5, while Condition C is only for AISC 360-22. On the other hand, when the slenderness ratio exceeds 1.5, buckling strength positively influenced by eccentricity Condition C and, Condition C provide higher buckling resistance than condition A for specimen sets 42 and 33, even.

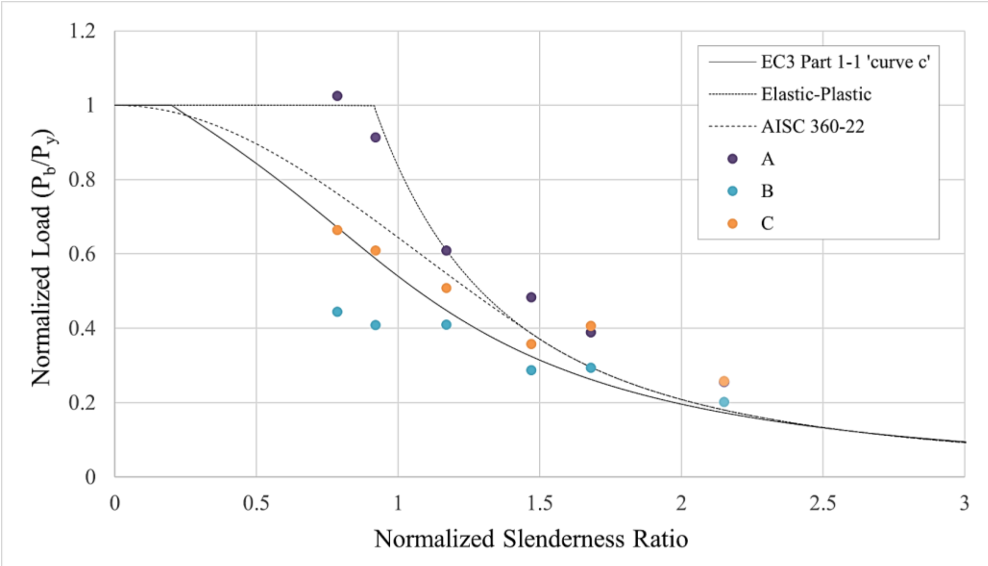

Figure 61. Comparison of normalized buckling load in FE analyses and design codes

To evaluate how different accidental eccentricity values (*0.5e* and *1.5e*) influence each series of models under equal (B) and unequal (C) eccentricity conditions a comparison was carried out. Comparisons were made based on a reference of *e* for each eccentricity condition. Separate comparisons were conducted for eccentricity conditions B and C in Figures 62 and 63, respectively. The same conclusion can be drawn from both charts where the application of a higher eccentric load leads to a reduction in the strength of the member and lower eccentricity leads to higher resistance. Additionally, it is observed that the impact of eccentricity value variation diminishes as the slenderness ratio increases. When evaluated in terms of design codes, while EC3 provides safe results for three different eccentricity ratios in Condition C, AISC does not provide such results. On the other hand, both design codes do not provide safe results for non-slender members in Condition B, regardless of the eccentricity ratio.

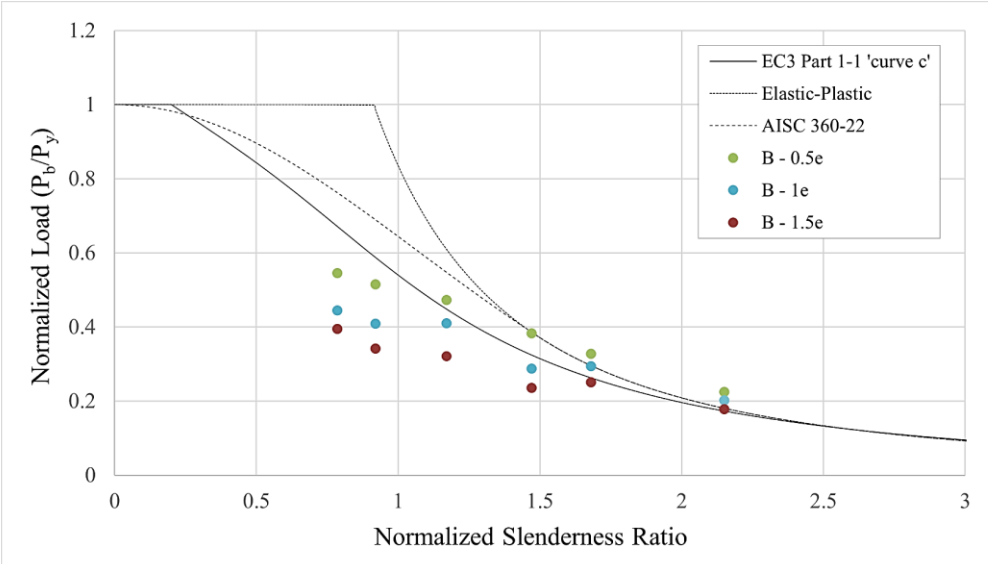

Figure 62. Comparison of eccentricity condition B at *0.5e* and *1.5e*

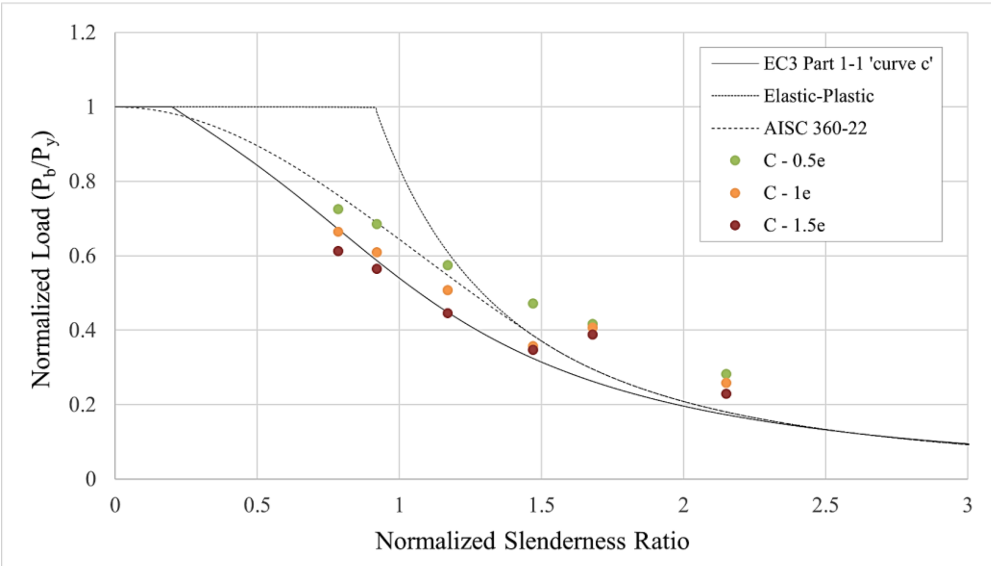

Figure 63. Comparison of eccentricity condition C at *0.5e* and *1.5e*

5. CONCLUSION

In this study the effect of various accidental joint eccentricity conditions on the behavior of concentric braces were investigated. Eccentricities which could be accidentally introduced were assumed to be very low to keep the whole cross section remains under compression forces. To do this, the magnitudes of the accidental eccentricities were determined with the sectional core area theory, also known as the cross-section kern. Four sets of brace specimens, each have different circular hollow sections with the same thickness but different diameters, were used to represent a range of global slenderness. Each set of specimens included three braces having the same cross section but different eccentricity conditions. Condition A represents centric loading (no eccentricity), condition B represents positive eccentricity at both ends (equal eccentricity) of the brace specimen, and condition C represents positive eccentricity on the top while negative on the bottom ends (unequal eccentricity) of the brace specimens. In the experimental studies, a total of 12 specimens were tested under cyclic loading, while in numerical studies, a total of 42 models were analyzed under cyclic loading. The results obtained from these studies, along with some recommendations, are presented below.

- The global buckling strength of the concentric braces varies depending on the eccentricity condition and the magnitude of joint eccentricity. As expected, as the magnitude of joint eccentricity increases, the buckling resistance decreases. However, in the case of equal joint eccentricity, the loss of global buckling strength is greater.
- In the case of equal eccentricity, concentric braces lose their compressive strength due to the bending effect, while in the case of unequal eccentricity, they lose strength due to buckling. Therefore, regardless of the slenderness ratio, a higher compressive strength can be achieved in the case of unequal eccentricity compared to the case of equal eccentricity.
- The effect of joint eccentricity on the compressive strength of concentric braces varies according to the slenderness ratio. According to experimental and numerical studies, the influence of joint eccentricity begins to be insignificant for both eccentricity conditions when the normalized slenderness ratio is greater than 1.5. However, when the normalized slenderness ratio is lower than 1.5, the effect of

joint eccentricity begins to be significant for both eccentricity conditions, and as the slenderness ratio decreases, it becomes even more important.

- Joint eccentricity, regardless of the slenderness ratio, leads to an increase in post-buckling strength in both eccentricity conditions. This is due to the straightening effect during tension cycles on the braces.
- Both eccentricity conditions do not lead to a significant difference in the fracture life and energy dissipation capacities of the concentric braces. However, it significantly reduces the initial stiffness, especially in the case of equal eccentricity.
- While AISC 360-22 (2022) does not yield sufficient results in either eccentricity condition, EN 1993-1-1 (2005) provides safe results only in the case of unequal eccentricity.
- Determining construction tolerances is necessary to reduce the effects of imperfections caused by accidental joint eccentricity. For this purpose, conducting similar experiments on sections with different geometries and slenderness ratios is recommended.

6. REFERENCES

Aghayere, A. O., & Vigil, J. (2020). *Structural steel design*. Mercury Learning and Information.

Albero, V., Ibáñez, C., Hernández-Figueirido, D., & Piquer, A. (2022). Experimental analysis on circular concrete-filled steel tubular beam-columns under unequal load eccentricities. *Engineering Structures, 259*, 114206.

American Institute of Steel Construction. (2022). *ANSI/AISC 303-22: Code of Standard Practice for Steel Buildings and Bridges*. Chicago, IL.

American Institute of Steel Construction. (2022). *ANSI/AISC 341-22: Seismic Provisions for Structural Steel Buildings*. Chicago, IL.

American Institute of Steel Construction. (2022). *ANSI/AISC 360-22: Specification for Structural Steel Buildings*. Chicago, IL.

ANSYS Inc. (2016). ANSYS (Version 15.0). Canonsburg, PA: ANSYS Inc.

British Standards Institution. (2006). *BS 7270: Metallic materials–Constant amplitude strain controlled axial fatigue–Method of test*.

Bruneau, M. (1998). Performance of steel bridges during the 1995 Hyogoken–Nanbu (Kobe, Japan) earthquake—a North American perspective. *Engineering Structures, 20*(12), 1063-1078.

Çayır, H., Vatansever, C., Yavaş, M. Ş., & Celep, Z. (2022). Eksenel Basınç Etkisindeki Çelik Elemanların Davranışında Geometrik Önkusurlar ve Artık Gerilmelerin Önemi [Importance of Geometric Imperfection and Residual Stresses on the Behavior of Steel Members Subjected to Axial Compression]. *Türkiye İnşaat Mühendisliği 18. Teknik Kongre ve Sergisi*, 7-9 November 2022, Istanbul.

Choi, B. H., & Yoo, C. H. (2005). Strength of Stiffened Flanges in Horizontally Curved Box Girders. *Journal of Engineering Mechanics, 131*(2), 167-176.

Cruise, R. B., & Gardner, L. (2008). Residual stress analysis of structural stainless steel sections. *Journal of constructional steel research, 64*(3), 352-366.

Debski, H., & Teter, A. (2019). Effect of load eccentricity on the buckling and post-buckling states of short laminated Z-columns. *Composite Structures, 210*, 134-144.

Demir, S., Ikram, M., Yılmaz, Y., & Soalih, H. (2024). Buckling and fracture behavior of cold formed carbon/stainless steel tubular braces under far field and near fault loadings. *Journal of Constructional Steel Research, 214,* 108444.

Elchalakani, M., Zhao, X. L., & Grzebieta, R. (2003). Tests of cold-formed circular tubular braces under cyclic axial loading. *Journal of Structural Engineering, 129*(4), 507-514.

Elghazouli, A. Y. (2003). Seismic design procedures for concentrically braced frames. *Proceedings of the Institution of Civil Engineers-Structures and Buildings*, *156*(4), 381-394.

European Committee for Standardization. (2004). *EN 1994-1-1:2004 Eurocode 4 - Design of Composite Steel and Concrete Structures - Part 1-1: General Rules and Rules for Buildings*. Brussels.

European Committee for Standardization. (2004). *EN 1998-1:2004 Eurocode 8 - Design of Structures for Earthquake Resistance - Part 1: General Rules, Seismic Actions and Rules For Buildings*. Brussels.

European Committee for Standardization. (2014). *EN 1993-1-1:2014 Eurocode 3 - Design of Steel Structures - Part 1-1: General Rules and Rules for Buildings*. Brussels.

European Committee for Standardization. (2016). *EN ISO 6892-1:2016 - Metallic materials - Tensile testing - Part 1: Method of test at room temperature*.

European Committee for Standardization. (2018). *EN 1090-2:2018 Execution of Steel Structures and Aluminium Structures – Part 2: Technical Requirements for Steel Structures*. Brussels.

European Convention for Constructional Steelwork (ECCS). (1986). *Recommended testing procedure for assessing the behaviour of structural steel elements under cyclic loads*. Brussels.

Goggins, J. M., Broderick, B. M., Elghazouli, A. Y., & Lucas, A. S. (2006). Behaviour of tubular steel members under cyclic axial loading. *Journal of Constructional Steel Research*, *62*(1-2), 121-131.

Guardiola Víllora, A. P. (2019). Central core of a rectangular cross section.

Han, S. W., Kim, W. T., & Foutch, D. A. (2007). Seismic behavior of HSS bracing members according to width–thickness ratio under symmetric cyclic loading. *Journal of Structural Engineering*, *133*(2), 264-273.

Harvey Jr, P. S., & Cain, T. M. N. (2020, February). Buckling of elastic columns with initial imperfections and load eccentricity. *Structures, 23*, 660–664. Elsevier.

Hernández-Figueirido, D., Romero, M. L., Bonet, J. L., & Montalvá, J. M. (2012). Ultimate capacity of rectangular concrete-filled steel tubular columns under unequal load eccentricities. *Journal of constructional steel research, 68*(1), 107-117.

Jönsson, J., & Stan, T. C. (2017). European column buckling curves and finite element modelling including high strength steels. *Journal of Constructional Steel Research, 128*, 136-151.

Kim, W. B. (2001). Ultimate strength of tube–gusset plate connections considering eccentricity. *Engineering Structures*, *23*(11), 1418-1426.

Klasson, A., Crocetti, R., & Hansson, E. F. (2016, November). Slender steel columns: How they are affected by imperfections and bracing stiffness. *Structures, 8*, 35–43. Elsevier.

Madah, H., & Amir, O. (2018). Concurrent structural optimization of buckling-resistant trusses and their initial imperfections. *International Journal of Solids and Structures, 162*, 244-258.

Saidani, M. (1998). The effect of joint eccentricity on the distribution of forces in RHS lattice girders. *Journal of Constructional Steel Research*, *47*(3), 211-221.

T.S.E. (2017). Steel and Steel Products - Location And Preparation of Samples and Test Pieces for Mechanical Testing. *TS EN ISO 377.* Ankara: Türk Standart Enstitüsü.

Tremblay, R. (2002). Inelastic seismic response of steel bracing members. *Journal of constructional steel research*, *58*(5-8), 665-701.

Ureña, A. G., Tremblay, R., & Rogers, C. A. (2021). Earthquake-resistant design of steel frames with intentionally eccentric braces. *Journal of Constructional Steel Research, 178,* 106483.

Ureña, A. G., Tremblay, R., & Rogers, C. A. (2022). Experimental and numerical study of square HSS BIEs under cyclic loading. *Engineering Structures, 252*, 113669.

Wang, C., Rudman, A., Tremblay, R., & Rogers, C. A. (2021). Numerical investigation into I-shape brace connections of conventional concentrically braced frames. *Engineering Structures*, *236*, 112091.

Wang, H., Wu, Q., Qian, H., Han, K., & Fan, F. (2019). Buckling behavior of a circular steel tube with a bolt–ball joint under installation eccentricity. *Engineering Structures, 197*, 109407.

Yoo, C. H., & Lee, S. C. (2014). *Stability of structures*. Woburn, MA: Butterworth-Heinemann.

Yoo, C. H., Choi, B. H., & Ford, E. M. (2001). Stiffness Requirements for Longitudinally Stiffened Box Girder Flanges. *Journal of Structural Engineering*, *127*(6), 705-711.

Zhao, J., Zhang, Y., & Lin, Y. (2014). Study on mid-height horizontal bracing forces considering random initial geometric imperfections. *Journal of Constructional Steel Research*, *92*, 55-66.

Zhou, F., Fang, C., & Chen, Y. (2018). Experimental and numerical studies on stainless steel tubular members under axial cyclic loading. *Engineering Structures, 171*, 72-85.

RESUME

Necip Sannah Upon completing his education in Syria, Necip received a YTB scholarship to pursue Civil Engineering at Kahramanmaras Sutcu Imam University. Graduating as the top student in the Faculty of Architecture and Engineering in 2021, he continues his academic journey with a focus on the "Effect of Accidental Joint Eccentricity on the Behavior of CHS Braces" for his Master's Degree in Civil Engineering Department at Karadeniz Technical University. He contributed to a project aimed at developing a seismic risk map for the Dulkadiroglu district during his tenure at Kahramanmaras Dulkadiroglu Metropolitan Municipality in 2021. Currently employed at Tekmetsan Demir Celik, he specializes in Structural Steel Fabrication and Construction since November 2023. Necip is proficient in Arabic, English, and Turkish languages.